Aalto University
School of Science
Degree Programme in Applied Physics

Konsta Särkimäki

Relativistic runaway electron simulations in 3D background

Master's Thesis
Espoo, October 7, 2015

Supervisor: Professor Mathias Groth
Advisor: Doctor Taina Kurki-Suonio

Aalto University
School of Science
Degree Programme in Applied Physics

ABSTRACT OF
MASTER'S THESIS

Author: Konsta Särkimäki

Title:
Relativistic runaway electron simulations in 3D background

Date:	October 7, 2015	**Pages:**	v + 66
Major:	Applied physics	**Code:**	F3005
Supervisor:	Professor Mathias Groth		
Advisor:	Doctor Taina Kurki-Suonio		

While the friction force in a plasma decreases with increasing test particle velocity, a particle can continue accelerating without limit once its velocity has exceeded the point where the friction and the accelerating forces are equal. In tokamaks, the toroidal electric field can result in electrons being accelerated. These so-called runaway electrons (RE) typically have energies ranging from 1 to 100 MeV, which make them highly relativistic. Important occurrence of REs is immediately after a plasma disruption where the rapidly cooling background causes the hot-tail of the electron population to become runaway. The number of REs is quickly multiplied when existing REs collide with thermal electrons. This avalanche process leads to the post-disruption plasma current to be carried entirely by REs which, in ITER, could lead to severe damage to the first wall when the plasma pulse terminates.

The RE phenomena and the means to mitigate the RE avalanche can be studied with orbit-following codes such as ASCOT. However, ASCOT lacked a suitable collision operator for relativistic particles as well as the radiation reaction force, both of which are essential for proper modeling. Therefore, a relativistic Fokker-Planck collision operator as well as the Abraham-Lorentz-Dirac force were implemented in ASCOT, and the theoretical background of these features as well as the implementation procedure are described in the thesis.

One of the proposed RE mitigation techniques is to cause REs to escape the plasma in a controlled manner by using magnetic perturbations. This thesis takes first steps in developing a simple model for collisionless radial transport in an externally perturbed magnetic field, where the field stochasticity induces the transport. The transport model involves drifting and diffusive transport, where the corresponding transport coefficients for a given field are evaluated with ASCOT.

Keywords: fusion energy, tokamak, runaway electrons, ASCOT, ITER, radial transport, plasma disruption

Language: English

Aalto-yliopisto
Perustieteiden korkeakoulu
Teknillisen fysiikan koulutusohjelma

DIPLOMITYÖN
TIIVISTELMÄ

Tekijä: Konsta Särkimäki

Työn nimi:
Relativististen karkurielektronien mallintaminen 3D taustassa

Päiväys:	7. lokakuuta 2015	**Sivumäärä:**	v + 66
Pääaine:	Teknillinen fysiikka	**Koodi:**	F3005
Valvoja:	Professori Mathias Groth		
Ohjaaja:	Tohtori Taina Kurki-Suonio		

Kitkavoiman suuruus plasmassa pienenee testihiukkasen kasvattaessa nopeuttaan, mikä johtaa rajoittamattomaan kiihtymiseen hiukkasen nopeuden ylittäessä arvon, jossa kitkavoima sekä kiihdyttävä voima ovat yhtäsuuret. Tokamakeissa ilmiö on havaittavissa toroidisuuntaisen sähkökentän kiihdyttäessä elektroneita. Näiden niin kutsuttujen karkurielektroneiden (KE) energia on tyypillisesti 1 ja 100 MeV välillä, mikä tekee niistä vahvasti relativistisia. KE:ta syntyy erityisesti nk. disruption yhteydessä, jossa taustan nopea jäähtyminen aikaansaa elektronipopulaation kuuman hännän karkaamisen. KE:ien lukumäärä moninkertaistuu nopeasti jo olemassaolevien KE:ien törmätessä termisten elektronien kanssa. Tämän lumivyöryprosessin seurauksena häiriönjälkeinen plasmavirta on kokonaan siirtynyt KE:ielle, mikä voi ITERssä johtaa vakavaan ensiseinämän vahingoittumiseen plasmapulssin tullessa päätökseen.

KE-ilmiötä sekä lumivyöryprosessin lievittämistä voidaan tutkia radanseurantakoodien kuten ASCOT:n avulla. ASCOT:sta kuitenkin puuttuivat sekä säteilyhäviöt että relativistisille hiukkasille pätevä törmäysoperaattori, jotka ovat kunnollisen mallintamisen kannalta välttämättömiä. Tämän vuoksi osana tätä työtä ASCOT:iin lisättiin sekä relativistinen Fokker-Planck törmäysoperaattori että Abraham-Lorentz-Dirac voima, joiden teoreettinen tausta ja toteutus koodiin ovat esiteltynä opinnäytetyössä.

Magneettikentän häiriöitä on ehdotettu yhdeksi keinoksi KE:en lieventämiseksi, sillä niillä voidaan aiheuttaa hallitusti KE:en häviöitä. Häiriöt tekevät kentästä stokastisten, jonka seurauksena KE:t kulkeutuvat radiaalisesti pois plasmasta. Työssä otetaan ensiaskeleet tätä kulkeutumista kuvaavan mallin kehittämiseksi. Kehitettävä malli sisältää ajautumisesta ja diffuusiosta johtuvan kulkeutumisen, joita vastaavat kuljetuskertoimet määritetään ASCOT:n avulla.

Asiasanat:	fuusioenergia, tokamak, karkurielektronit, ASCOT, ITER, radiaalinen kulkeutuminen, plasmahäiriö
Kieli:	Englanti

Acknowledgements

I feel privileged to be able to spend my days doing things that I enjoy while also getting paid. This is more than I deserve and I am extremely grateful for the people that have made this possible. I would like to thank my supervisor, professor Mathias Groth, for his guidance and for enduring the extra bureaucratic burden I have caused. My advisor Taina Kurki-Suonio had to spend both of her vacations on proof-reading my thesis, and I thank her for her dedication and advice. But more than that, I like to congratulate her for being an excellent leader for our research group. I have really enjoyed the independence, the challenges, and the good mood I am sure I would have not been able to experience anywhere else.

Speaking of our group, buckets of gratitude goes to my co-workers, two of which deserve special merit. Simppa Äkäslompolo has helped me with every problem, both big and small, and had always time for explaining things that I was too young to understand. Eero Hirvijoki, who has already left the building, has been a constant source of new ideas and challenges. Following in his footsteps has taught me a great deal about plasma physics. I would also like direct my thanks to professor Joan Decker, whom I visited with Jari Varje and Eero during last spring. Discussions with Joan and doctor Gergely Papp contributed to this thesis significantly. This work was funded by Fusion For Energy Grant 379 and the Academy of Finland project No. 259675.

Finally, I would like to thank the person that has supported me most in my life, not only financially but, more importantly, also providing wisdom that has guided me thorough my life. Dad, exercise and eat healthily. It is important for me that you will be present at my defence of dissertation at couple of years from now.

Espoo, October 7, 2015

Konsta Särkimäki

Contents

Chapter 1

Introduction

Fusion energy is the crown jewel of the centuries of humanity's scientific and technological advancement. It has been a physicist's dream ever since the starry night in 1920's, when Fritz Houtermans proclaimed to his girlfriend that, at that moment, he is the only person in the world who knows why the stars shine, having discovered the thermonuclear processes taking place in stars' core earlier that day. This dream, however, has turned out to be nightmarishly difficult. Through the history of the fusion energy research, one of the main ideas to achieve laboratory fusion has been to apply a magnetic field to confine the hot ionized gas, i.e., the plasma, where the fusion occurs. The first devices to explore this idea were linear *magnetic mirrors*, which soon evolved to circular *stellarators*, where the field lines are closed. With these devices, the fusion energy was meant to provide "energy too cheap to meter" but the early optimism was quickly lost when it emerged that plasma losses were unacceptably high in both concepts [1]. However, these losses were greatly reduced with the invention of the *tokamak* in 1950's. Since then, the progress has been rapid, and the first fusion reactor ITER, which will finally demonstrate fusion as a viable energy source, is currently being built [2]. ITER greatly exceeds todays fusion experiments in both physical size and complexity as it scopes to achieve fusion power output of 500 MW during a pulse that lasts several minutes. Developing materials that can withstand resulting power fluxes is a difficult quest on its own but more difficulties are brought by the amount of energy contained within the plasma and the magnetic field. These poise challenges that cannot be fully studied in todays experiments and the fate of ITER rests heavily on predictions made by computer simulations.

1.1 Runaway electrons

One important challenge arises from an extraordinary nature of the friction force in a plasma. For plasma particles with low velocities, the friction force grows with increasing speed, which is a familiar effect for every cyclist. Where the friction in plasma differs from the drag experienced by the cyclist is that the former has a global maximum after which it starts decreasing with increasing particle velocity as Fig. 1.1 illustrates. This behavior, which is due to the nature of the Coulomb collisions [3], can lead to a situation where the particle can accelerate freely if the accelerating force itself does not depend on the velocity. In practice, this can happen in the presence of an electric field that is parallel to the magnetic field. If the conditions are suitable, electrons, as they move much faster than ions, could overcome the friction force, thus becoming so-called *runaway electrons* (REs). These electrons can reach energies from 1 to 100 MeV, making them highly relativistic.

Even though the friction force decreases, it will not vanish completely as Fig. 1.1 shows. Therefore, there exists a minimun electric field required for the existence of runaway electrons. This *critical field* is given as [4]

$$E_c = \frac{n_e e^3 \ln \Lambda}{4\pi \epsilon_0^2 m_e c^2}, \tag{1.1}$$

where n_e is the electron density, e is the elementary charge, $\ln \Lambda$ is the Coulomb logarithm, ϵ_0 is the vacuum permittivity, m_e is the electron mass, and c is the speed of light in vacuum. As the friction force has a global maxima, increasing electric field strength will eventually lead to all electrons being runaways. The electric field value after this happens is the *Dreicer field*

$$E_D = \frac{n_e e^3 \ln \Lambda}{4\pi \epsilon_0^2 T_e}, \tag{1.2}$$

where T_e is the electron temperature. Equation (1.2) should, however, only be taken as a purely theoretical concept; when the bulk electrons gain speed, also the friction force is affected, and these equations no longer hold. Even though the friction loses its importance at high velocities, there are other loss mechanisms preventing the particle energy from growing boundlessly. One important mechanism is the cyclotron emission arising from the particle gyromotion, whose magnitude is proportional to the particle velocity perpendicular to the magnetic field. Therefore, the maximum RE energy depends on both electric field and the particle pitch, i.e., the fraction of the velocity that is parallel to the magnetic field. Figure 1.2 depicts this dependence in ITER-like conditions.

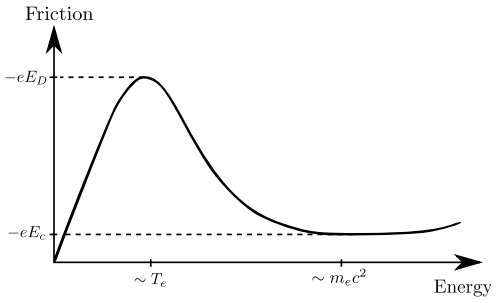

Figure 1.1: Friction force as a function of electron energy [5]. E_c is the minimum electric field which is required for runaway generation, and E_D is the limit after which all electrons become runaway.

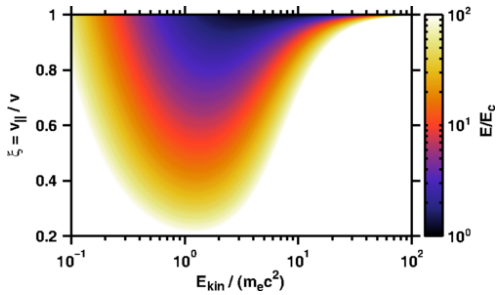

Figure 1.2: Allowed runaway electron energies at given electric field and particle pitch [6].

The electric field alone cannot generate REs but only sustain those that exist. There are a few mechanisms that can push a thermal electron to the runaway regime [7]. The so-called *Dreicer mechanism* is the collisional process that diffuses electrons to the hot tail of the Maxwellian distribution where they can become runaways. A closely related mechanism is a sudden cooling of a plasma, where the hot tail electrons do not get to lose their energy fast enough so the vanishing friction transfers them to the runaway regime. Energetic electrons are also produced when activated wall material releases gamma radiation, which transfers energy to plasma electrons via Compton scattering. Yet another source is the beta decay of tritium but these two latter mechanisms will only be significant in ITER and other next generation tokamaks. Once a RE population is born due to one or more of these *primary mechanisms*, more runaways are produced when the existing ones collide with thermal electrons. This is the *secondary mechanism* for runaway generation. If the colliding electron has enough momentum to transfer the target electron to the runaway regime while retaining enough to stay there itself, these collisions can quickly lead to a multiplication of the number of REs. This *runaway electron avalanche* can lead to an incident where large amount of energetic electrons are generated and sustained until the end of the plasma pulse, when they escape the plasma with detrimental results.

The possibility of a RE generation is inherently present in tokamaks as long as the plasma current is induced with an electric field. As the electric field is toroidal, it lies almost parallel to the magnetic field and the electrons are able to accelerate along it. However, the runaway generation is usually suppressed by the high plasma density, as we can see by substituting typical

ITER parameters ($n = 10^{20}$ m^{-3}, $\ln\Lambda = 10$) into Eq. (1.1). This gives $E_c = 0.05$ V/m, which is higher than the typical ITER toroidal electric field of 0.02 V/m. Therefore, runaways are only produced during plasma disruptions and current ramp-up phase when the density is lower and the electric field higher. REs generated during ramp-up are called *reverse runaway electrons* and they were problematic for early tokamaks as their presence hampered the efficiency of the plasma current induction [8]. Compared to disruption-generated REs, the reverse runaways are only a minor annoyance. Post-disruption RE population grows via avalanche mechanisms to a point where the plasma current is completely formed by REs. After the confinement is lost, the RE beam strikes the first wall in an uncontrolled manner which can cause power fluxes exceeding design parameters of the wall material. The number of REs that are generated scales exponentially with the plasma current so these could poise a serious threat to ITER [9]. Current RE studies are primarily focused on understanding the disruption-generated REs and finding a way to prevent the formation of the RE beam [10–12]. This thesis focuses on the runaway phenomena during the disruption only.

Even without REs, plasma disruptions in tokamaks are violent events [13] that, in the best case, only terminate the plasma discharge. At worst, they cause serious damage to reactor components. To avoid the latter possibility, disruptions are mitigated by, for example, injecting pellets which transfer energy safely from the plasma via radiation [14]. Unfortunately, this also causes REs to be born. Whether a disruption is mitigated or not, plasma cools down fast, faster than the collision time of energetic electrons in the tail of the Maxwellian distribution. Therefore, these electrons are not immediately thermalized but conserve their high energy. As the plasma cools down, resistivity, and therefore the electric field, increases and the non-thermalized fast electrons become runaway. These runaways then provide the seed population for the avalanche mechanism. In order to prevent the formation of the post-disruption RE beam, the seed population must be either thermalized or removed from the plasma. The thermalization could be achieved by injecting impurities into the plasma whereas RE losses could be induced by introducing magnetic perturbations, thus taking advantage of the REs' sensitivity to magnetic field structure. However, neither of these mitigation techniques are successful in ITER at their current state. Furthermore, the runaway phenomena itself is not well understood: radial transport of REs [15], energy and pitch distribution [16], and even the radial profile [17] of the RE beam remain open questions.

1.2 Structure of this thesis

Understanding RE transport is critical for developing mitigation techniques for ITER. Therefore, this work aims to develop means for studying this phenomena in realistic 3D magnetic fields. Our focus is on the Monte Carlo code ASCOT which is a capable tool for minority particle population studies in tokamaks [18]. ASCOT has been used extensively for fast ion research and it contains the means for a realistic particle following, including test particle collisions with both background plasma and a 3D wall. Furthermore, ASCOT could provide an unique tool for investigating impact locations and wall loads of runaway beams in ITER (and other tokamaks) as the code contains a detailed 3D model of the ITER first wall (among others). However, it lacks some necessary physics for runaway electron modelling which are implemented as a part of this thesis. With the runaway electron physics included, ASCOT can be employed for studying RE transport in 3D background and investigating how realistic magnetic field affects the RE behavior in phase-space. In this thesis, we adopt ASCOT in exploring whether a simple model, where the field complexity is reduced to just one radial coordinate, could replicate the RE radial transport.

New physics have to be included to ASCOT since REs, having smaller mass and greater energy, are even faster than the fusion-born alpha particles. Whereas cyclotron radiation emission can be neglected for ions, it becomes increasingly important at higher velocities and, as noted earlier, sets an upper limit for the RE energy. Furthermore, REs are (ultra)relativistic as $\mathcal{E}_{kin} \gg m_e c^2$, and relativistic treatment can no longer be neglected. ASCOT already contains relativistic equations of motion, but collisions have been nonrelativistic so far. This disparency is eliminated by implementing the relativistic Fokker-Planck collision operator. This thesis work still omits *bremsstrahlung* and *knock-on collisions*, which are left for future work. The knock-on collisions are the driving mechanism for the runaway electron avalanche and they result in a large scattering angle. Therefore, they differ significantly from the small scattering angle collisions that are typical in plasma. The knock-on collisions are omitted as they cannot be modelled with Fokker-Planck collision operator. Including bremsstrahlung can be important once one wishes to study RE mitigation with impurity injection, but this mitigation technique will not be investigated in this thesis.

This thesis is structured as follows. Chapter 2 contains a review of the runaway electron phenomena during tokamak disruptions. There we will also discuss the open questions regarding the RE transport. Chapter 3 introduces the guiding center formalism which is a necessary tool for an efficient particle

following. There we present the mathematical foundation for evaluating the guiding center motion. The actual physics are separated to the following chapter. Therefore, readers that are already familiar with the guiding center formalism and relevant coordinate transformations, can skip to chapter 4 where the relativistic equations of motion, radiation losses, and collisions are evaluated in both particle and guiding center phase space. Implementation of the missing features into ASCOT is described in chapter 5, and their importance is discussed. Finally, RE radial transport is studied with the enhanced ASCOT code in chapter 6.

Chapter 2

Runaway electrons in plasma disruptions

Before proceeding to discuss disruption-generated RE phenomena, a brief review of plasma disruptions in tokamaks is given. A fusion plasma stays in a stable equilibrium only as long as the magnetic and kinetic pressures balance each other. A *disruption* begins once a magnetohydrodynamics (MHD) instability causes tokamak plasma to exit the stable region of its operational parameters [13]. The resulting *vertical displacement event* (VDE) causes the plasma to be deposited on the reactor wall in milliseconds. The reactor volume and, hence, energy content of the plasma is roughly proportional to the cube of the major radius, whereas the wall area is only proportional to its square. Therefore, the possibility of the plasma depositing its thermal energy to the first wall must be taken seriously in larger tokamaks. Furthermore, VDE results in *halo currents* that are induced in the first wall. The halo currents release the magnetic energy of the plasma, and the resulting $\mathbf{j} \times \mathbf{B}$ forces cause mechanical stress to vessel components. Again, this is a serious event in larger tokamaks; halo currents have been shown to result in large forces leading to vessel displacements of several millimeters in JET [19].

To avoid the uncontrolled release of thermal and magnetic energy in ITER, impurities with high charge number, Z, will be injected to the plasma as a pre-emptive action when the disruption prediction systems indicate that a disruption is imminent. Impurities cause the plasma to radiate its energy safely before the disruption begins [20–22], thus mitigating the consequences of the disruption. Impurity injection via pellets, known as the *killer pellets*, have been shown to reduce the heat loads to the vessel wall by 90 %, and also to reduce the halo currents by 50 %. The other method is a massive gas injection (MGI) where a gas burst, amounting to several times more particles than contained within the plasma, is deposited to the reactor chamber.

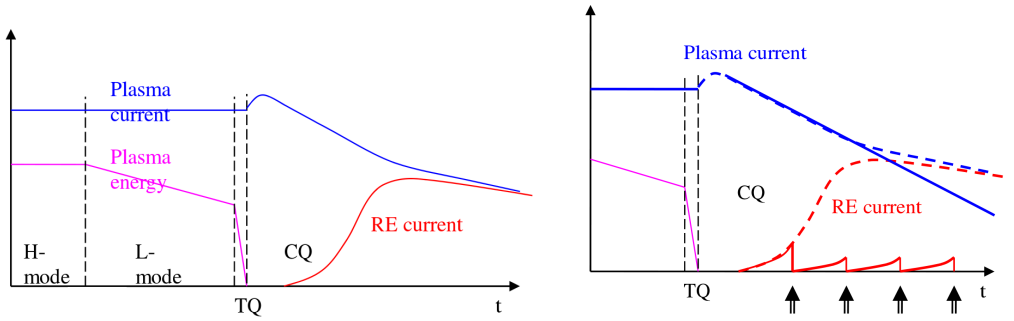

Figure 2.1: A plasma disruption event [24]. Time-axis is in the order of twenty milliseconds. (a) Time-evolution of the plasma current and energy. The peak in the plasma current is due to MHD instability unrelated to runaway generation. (b) Accumulation of the runaway current mitigated via repetitive gas injections indicated by the arrows.

Regardless which mitigation method is used, a successful mitigation of the disruption leads to a rapid cooling of the plasma [23]. This event is appropriately named the *thermal quench* (TQ) as, e.g. in ITER, the plasma temperature is expected to fall below 1 keV in less than 1 ms. Both impurities and low plasma temperature lead to an increase in resistivity which is followed by a *current quench* (CQ), i.e., a fast deterioration in plasma current. The current quench in ITER lasts for about 40 ms, during which REs become significant as depicted in Fig. 2.1a. In other words, we have a "out of the frying pan, into the fire"-kind of situation: disruption mitigation leads to RE generation, which in turn has to be mitigated.

2.1 Evolution of the runaway electron current

The generation of the RE current begins when the rapid cooling during TQ results in a small RE population which is then amplified by the avalanche mechanism [25]. Runaways are also produced continuously by the Dreicer mechanism, but at much smaller rate compared to the avalanche process. The increase in runaway population, together with the increased resistivity for thermal electrons, are the reasons for the dominant role REs have in the remaining plasma current. The production of the runaways diminishes the toroidal electric field and, therefore, the current eventually reaches a post-

disruption steady state (in the absence of losses) where all current comes from REs. ITER, if REs are unmitigated, is expected to have an post-disruption plasma current of 70 % of the pre-disruption value which, in the baseline scenario, translates to a runaway current of 12 MA carrying 10 MJ of kinetic and 200 MJ of magnetic energy [24]. When the plasma pulse is terminated at the end of the disruption, runaways exit the plasma as a focused highly-energetic beam which can melt the plasma facing components [26].

Energy content of the runaway population scales with the plasma current, and mitigation schemes to limit the runaway current below 2 MA in ITER need to be developed [24]. Although no proven mitigation method exist yet, the runaway electrons can be mitigated in principle by either increasing the collisionality, or suppressing the growth rate of the runaway electron avalanche. The former could be performed with another MGI, which would increase electron density, but the amount of gas that would have to be injected is too large. Injecting particles into cold, low-density plasmas could lead into the injected gas being deposited to the walls, the gas passing the plasma without interaction. Furthermore, another MGI would cool the plasma even further, which shortens the CQ time, causing more mechanical stress to vessel components.

The growth rate is suppressed when the runaways are lost at the same rate as new ones are generated by the collisions. There are several proposals on how to achieve this; however, none of them are proven yet. Losses can be increased by introducing magnetic perturbations either via external coils or with repetitive injections of gas [24] (not to be confused with the MGI scheme introduced earlier). ITER hosts ELM coils, intended for mitigating violent ELMs, which could be used also in the post-disruption phase to generate magnetic perturbations. However, the ELM coils are probably too weak for this purpose as they can cause RE losses on the edge region only [15], whereas most of the runaways are expected to be found near the core where the magnetic field is almost toroidal. Repetitive injection of gas to rational flux surfaces seems more promising as the required amount of gas during one injection is one tenth of that required for the previously described scheme where the collisionality is increased. The principle of this repeatitive-injection method is illustrated in Fig. 2.1b.

If runaways are not mitigated, their effect is not limited to the possibility of wall damage. The RE dominance over the plasma current could have implications for post-disruption MHD stability. Furthermore, evolution of the toroidal electric field and RE population are coupled to each other. In the absence of losses, time-evolution of the RE population has been computed self-consistently taking evolving electric field into account [17], resulting in profiles shown in Fig. 2.2. The runaway generation via avalanche mecha-

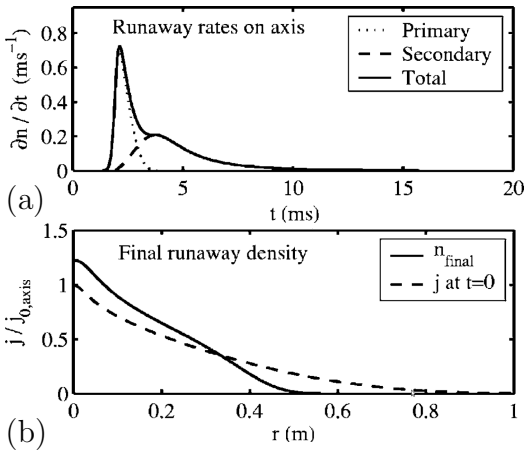

Figure 2.2: Simulated RE profiles during a JET discharge [17]. (a) Runaway generation rates via primary and secondary mechanisms after the disruption. (b) The final runaway density compared with initial current profile.

nism becomes dominant after TQ as the primary generation mechanisms are more sensitive to the electric field strength. The primary generation mechanisms still affect the final current profile as they provide the seed population which is then multiplied by the avalanche mechanism. In ITER and other devices where TQ is rapid (temperature decreases exponentially with a decay coefficient $t_{exp} < 0.03$ ms), the hot tail mechanism is dominant over the Dreicer mechanism in the generation of the seed population [7]. The results in Fig. 2.2 indicate that the spatial profile of the runaway current deviates significantly from the plasma current profile before the disruption. The post-disruption current is more peaked at the core to the extend it actually has a larger magnitude there than the pre-disruption current. The current profile confirms that most of the RE population is found near the core, which makes RE mitigation via growth rate suppression difficult.

Before proceeding to discuss radial transport of REs, a short review of how information about REs can be gathered is relevant. REs emit radiation via synchrotron, cyclotron and bremsstrahlung processes [27]. The *synchrotron radiation* is emitted when an electron follows its toroidal trajectory, the emission being directed along the particle velocity vector. This radiation can be used to measure velocity distribution of the RE population and to obtain, e.g., the maximum RE energy [16]. The *cyclotron radiation*, arising from particle gyromotion, is not nearly as useful in terms of measurement since REs have pitch values close to unity, resulting in weak emission. Furthermore, the plasma strongly absorbs radiation emitted in this frequency. *Bremsstrahlung* from collisions with ions (and electrons) result in *soft* X-rays ($\sim$ 1 - 10 keV)

but, more importantly, collisions with plasma facing components produces *hard* X-rays (> 10 keV) which reveal information about RE beam strike points. The strike points can also be identified with infrared camera due to deposition of beam energy. Experiments at JET have revealed that RE beams strike the first wall at the upper dump plates in toroidally localized hotspots [28]. Interestingly, the beams were observed to strike in pulses with a 1 ms pause between consecutive pulses. This has led to a hypothesis that the radial profile of the runaway current is filamental due to its sensitivity on plasma parameters [17].

2.2 Radial transport

Runaway electron losses due to field perturbations in ITER have been studied with test particle simulations [15, 29]. The main findings are shown in Figs. 2.3a and 2.3b. The simulations revealed that REs originating from $\rho > 0.7$ (normalized) poloidal flux surfaces are lost between 10 - 11 ms in the unperturbed case. With ELM coil induced perturbation, 95 % of the total particles from $\rho > 0.7$ surface were lost within 0.1 ms and the rest after 2 - 3 ms. The time during which particles were lost displayed a strong radial dependence. Even with perturbations, the REs inside the $\rho = 0.5$ surface were well-confined so the avalanche is suppressed only near the edge. Notably, the perturbation caused the losses to be toroidally localised which could lead to significant wall loads even in the absence of the avalanche. However, one must take care in interpreting these result as the self-consistent treatment of the electric field and runaway electrons is absent.

Even though simulations were performed with ELM coils that are unlikely to be used for this purpose, these results give valuable insight to other perturbation-based mitigation schemes. For example, these results revealed that perturbation strength of $\delta B/B > 10^{-3}$ is necessary to generate significant losses, which is confirmed by other studies as well [9]. The complete picture is more complicated as the structure of the perturbed magnetic field, not the perturbation strength alone, determines which particles are lost as indicated in Fig. 2.3a. The perturbation causes field lines to become chaotic near the plasma edge which leads to collisionless particle losses. Closer to the core, magnetic islands are formed which confine particles effectively. These results emphasise the sensitivity of the runaway losses with respect to applied perturbation.

Usage of test particle codes in other areas of fusion research, such as fast ion physics, is warranted but their use is limited in the runaway electron physics as the runaways are tightly coupled to the evolution of the parallel

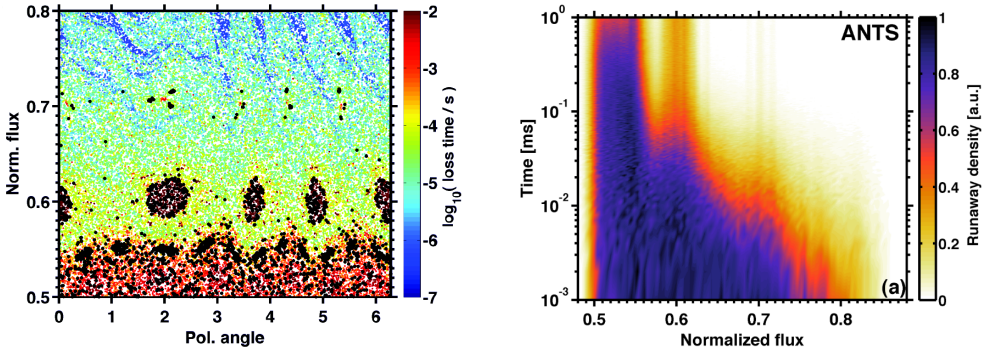

(a) (b)

Figure 2.3: ELM coil induced RE losses simulated with ANTS [15]. (a) Initial distribution of the runaway electrons colored with the loss time. (b) Time-evolution of the RE density profile.

electric field. Self-consistent treatment of runaway electron population can be performed with codes such as LUKE [30], GO [31], and ARENA [32] but these have their own limitations. One restriction is that they are limited to one spatial dimension, i.e., these codes only consider radial coordinate. This restraint means that 3D effects affecting RE transport, such as the toroidal field ripple and magnetic perturbations, are missing unless they are incorporated as an extra transport term. In order to obtain complete picture of the RE transport, test particle codes should be employed to compute the effective radial transport in a 3D background which is then supplied to codes solving the RE population consistently.

Theoretical analysis of the radial transport stems from the fact that REs, being extremely collisionless, are affected predominantly by the magnetic field structure. Transport in a stochastic field can be viewed as a diffusive process (even though trajectories of individual particles are completely deterministic) with the *Rechester-Rosenbluth diffusion coefficient* [33],

$$D_{RR} = \pi \bar{q} R \left(\frac{\delta B}{B} \right)^2 , \tag{2.1}$$

where $\bar{q}$ is the safety factor and R is the major radius. Reicester-Rosenbluth diffusion models the diffusion of a stochastic magnetic field itself, and the particle diffusion coefficient is obtained by multiplying the coefficient D_{RR} with the parallel velocity of the particle. For REs, the parallel velocity is approximately the speed of light, and we obtain $D_{RE} \approx cD_{RR}$.

However, the simulations of RE transport in ITER found that the transport, depicted in Fig. 2.3b, is not proportional to $(\delta B/B)^2$ which invalidates

the Rechester-Rosenbluth diffusion. Furthermore, the study claims that the nature of the transport is not diffusive at all. The authors devised a qualitatively different model to depict the transport in the case being studied, but a general model for RE radial transport does not exist. The main difficulty arises from the complex nature of the field as the field contains magnetic islands and confined field lines along with the stochastic region, where field lines end up to the wall. The transport model should be able to account for the particles confined in the islands while still modeling transport in the stochastic region accurately. Furthermore, the wall should be treated as a sink, since REs ending up there are lost. The confined region should form a barrier from which REs are reflected as the particle cannot cross the confined-nonconfined boundary when there is no change in particle energy. One should also keep in mind that, while REs follow field lines quite faithfully, there is a small deviation from the field line if the pitch does not equal to unity. Even with unit pitch, highly energetic REs drift strongly from their initial field line.

Chapter 3

Introduction to guiding center formalism

A common practice in test-particle codes is to employ the so-called *guiding center formalism*[34] where motion of a charged particle in a magnetic field is taken as a superposition of three components with distinct timescales. The motion perpendicular to the field is reduced to a fast circular motion while the *guiding center*, the center point of the circling, moves along the same field line. The third component arises from the magnetic field nonuniformity (and also from a perpendicular electric field if present) which leads the guiding center to drift slowly from the field line while still preserving the much faster gyromotion. These components are illustrated in Fig. 3.1.

What exactly do we mean when we say that the cyclotron motion is "fast" and the drift is "slow"? The timescales associated with the three components of motion may be estimated as follows. The cyclotron motion is a periodic motion whose frequency is given by the *gyrofrequency* $\omega_g \equiv |q|B/m$. Here B is the magnetic field strength, and m and q are the particle charge and mass respectively. For example, an electron in a magnetic field of $B = 1$ T will oscillate at frequency $\omega_g = 2 \times 10^{11}$ Hz. A similar periodic motion can be identified for the parallel component when the particle travels along a poloidally closed loop in an axisymmetric toroidal magnetic field. The frequency associated with this poloidal motion is called *bounce frequency* which is given by $\omega_b \equiv v_\parallel/r$ where $v_\parallel$ is the particle velocity parallel to the field and r is the minor radius. Modern tokamaks have typically $r \approx 1$ m, and we can use the speed of light for the parallel velocity to obtain the upper estimate $\omega_b = 3 \times 10^8$ Hz. Estimating timescale of the drift motion is more elaborate as it has no associated periodic motion. However, we can compute the drift velocity and compare it to the minor radius in a similar manner as was done for the parallel velocity to obtain an order of magnitude estimate.

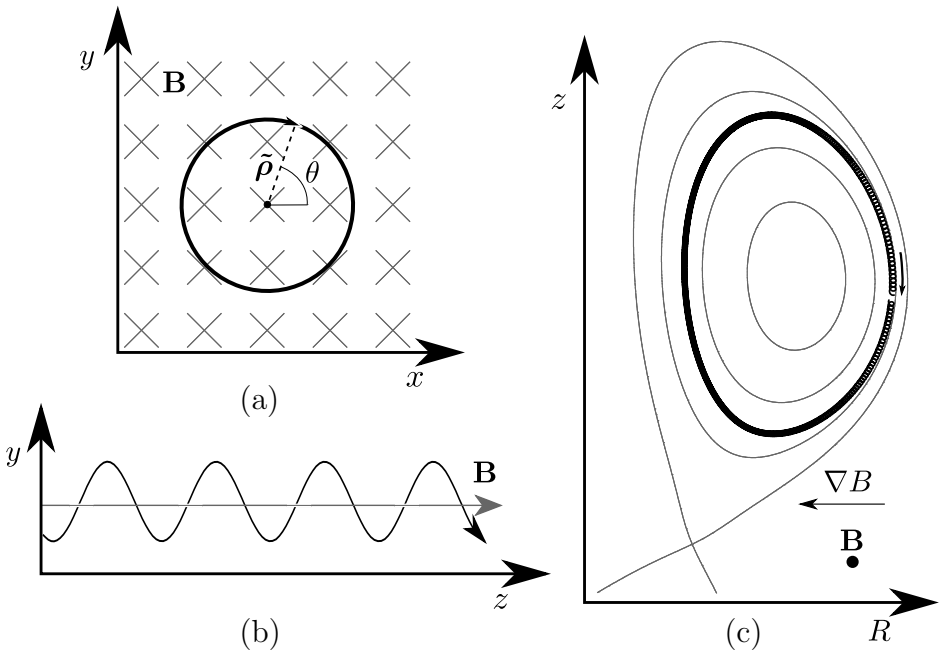

Figure 3.1: Illustration of the three different components of a particle motion. In a uniform magnetic field, the motion consists of (a) fast cyclotron motion in a plane perpendicular to the field and (b) motion parallel to the field. Here $\tilde{\boldsymbol{\rho}}$ and θ stand for gyroradius and gyroangle respectively. Magnetic field nonuniformity causes slow drift as shown in (c), where the trajectory is projected on a poloidal plane. Here, grey curves are contours of poloidal flux coordinate.

Drift due to a variation in the magnetic field strength, the *grad B drift*, is given by

$$\mathbf{v}_d = \frac{\mathcal{E}_\perp}{qB} \frac{\mathbf{B} \times \nabla B}{B^2}, \tag{3.1}$$

where $\mathcal{E}_\perp$ is the perpendicular kinetic energy. In tokamaks, the toroidal component of the total field is dominant so that the magnetic field is almost parallel to the gradient, i.e., $\mathbf{B} \perp \nabla B$. For the minor radius of one meter, we can make an estimate $\nabla B/B \approx 1$ m^{-1}. Assuming we have a very fast electron with all of its energy in the perpendicular motion $\mathcal{E}_\perp = 1$ MeV, we get $v_d = 1 \cdot 10^6$ m/s from Eq. 3.1. This will give us the "drift frequency" $\omega_d = 1 \cdot 10^5$ Hz. As we can see, cyclotron motion is six orders of magnitude faster than the drift motion.

The benefit of the guiding center formalism is apparent: by focusing on the guiding center motion, the rapid gyromotion can be omitted while still keeping track of the particle trajectory. However, the guiding center

approximation is valid only in plasmas where the particle is able to complete its gyro-orbit uninterrupted and the gyroradius does not vary strongly during one gyrophase. The gyromotion is interrupted when the particle experiences collisions that alter its trajectory significantly. Therefore, the first condition is satisfied when the collision frequency is less than the gyrofrequency. The second condition is satisfied when the magnetic field does not vary strongly in a length scale comparable to the gyroradius. Both these conditions generally hold in ITER-like plasmas.

As this thesis aims to present practical numerical schemes for runaway electron simulations, the guiding center formalism will naturally be applied. This chapter functions as an introduction to the guiding center formalism and related mathematical methods found in literature. Many theorems in this chapter are only briefly discussed, therefore interested reader is guided to Refs. [34–37] for more in-depth view.

3.1 From particle phase space to guiding center phase space

The particle state is well-defined if both its *position* $\mathbf{x}$ and *momentum* $\mathbf{p}$ are known. Therefore, we can say that the coordinates $(\mathbf{x}, \mathbf{p})$ form the *particle phase space*. However, the momentum component parallel to the magnetic field behaves differently than the other components due to the gyromotion: when particle travels along the field the parallel momentum varies slowly whereas perpendicular component oscillates rapidly due to the cyclotron motion. We can take this anisotropic behavior into account by choosing new coordinates to represent the particle phase space. First, we decompose $\mathbf{p}$ to its parallel and perpendicular components

$$\mathbf{p} = p_\parallel \hat{\mathbf{b}} + \mathbf{p}_\perp, \tag{3.2}$$

where $\hat{\mathbf{b}}$ is an unit vector pointing along the magnetic field. Choosing fixed orthogonal basis $\{\hat{\mathbf{e}}_1, \hat{\mathbf{e}}_2\}$, where $\hat{\mathbf{b}} \times \hat{\mathbf{e}}_{1,2} = 0$, and notating *gyroangle* with θ, we can express the perpendicular momentum as

$$\mathbf{p}_\perp = p_\perp \left(-\sin\theta \hat{\mathbf{e}}_1 + \cos\theta \hat{\mathbf{e}}_2\right). \tag{3.3}$$

Finally, defining the *pitch* variable as $\xi \equiv p_\parallel / p$, we arrive at

$$\mathbf{p} = \xi p \hat{\mathbf{b}} + \sqrt{1-\xi^2} p \left(-\sin\theta \hat{\mathbf{e}}_1 + \cos\theta \hat{\mathbf{e}}_2\right), \tag{3.4}$$

which allows us to express the particle phase space in $(\mathbf{x}, p, \xi, \theta)$ coordinates.

Now that the momentum coordinate $\mathbf{p}$ is successfully adjusted to take the gyromotion into account, we can proceed to process the spatial coordinate $\mathbf{x}$. Notating *guiding center position* with $\mathbf{X}$, we have

$$\mathbf{x} = \mathbf{X} + \tilde{\boldsymbol{\rho}}, \tag{3.5}$$

where $\tilde{\boldsymbol{\rho}}$ is the *gyrovector*. If we are uninterested in the exact position of the particle, we can leave out $\tilde{\boldsymbol{\rho}}$ thus obtaining the *guiding center phase space* $(\mathbf{X}, p, \xi, \theta)$.

An alerted reader may have noticed that the gyroangle θ is still present in our choice of the guiding center phase space coordinates. However, having θ included in our phase space coordinates is not forbidden as long as the guiding center equations of motion themselves will be independent of the gyroangle. θ could be omitted but we decide to keep it since $\dot{\theta}$ will be present in the guiding center Hamiltonian accounting for the energy associated with the gyromotion.

Of course, there are other valid coordinate systems for presenting the guiding center phase space. For example, the equations of motion in guiding center phase space are usually expressed in coordinates $(\mathbf{X}, p_\parallel, \mu, \theta)$ where the *magnetic moment* μ is defined as

$$\mu \equiv \frac{\frac{1}{2}p_\perp^2}{mB} = \frac{(1-\xi^2)\,p^2}{2mB}. \tag{3.6}$$

The reason is that μ is an adiabatic invariant: in slowly varying magnetic fields μ stays constant. However, this holds only if both collisions and radiation losses are omitted. Regarding collisions, the coordinates $(\mathbf{X}, p, \xi, \theta)$ are useful as the collision operator will have a diagonalizable form in these coordinates, as will be shown later.

3.2 Review of noncanonical Hamiltonian mechanics

The dynamics of any system is contained in its Lagrangian form from which the equations of motion are extracted with the Euler-Lagrange equation. Alternatively, system can be described by its Hamiltonian and the Hamilton's equations are utilized to find the equations of motion. Hamiltonian mechanics taught for the second-year physicists generally employ *canonical formalism*, which requires that condition

$$\mathbf{p} = \frac{\partial L}{\partial \bar{\mathbf{q}}}, \tag{3.7}$$

where $L(\bar{\mathbf{q}}, \bar{\mathbf{p}})$ is the *Lagrangian*, must hold. The variables $\bar{\mathbf{q}}$ are the *generalized coordinates* and $\bar{\mathbf{p}}$ the *generalized momenta* which together form the phase space $(\bar{\mathbf{q}}, \bar{\mathbf{p}})$. The particle phase space coordinates consisting of position and momentum obviously meet the condition (3.7) and one may proceed to use the canonical Hamiltonian dynamics. However, neither of the guiding center phase space coordinates we would like to utilize meet this requirement. Thus, employing *noncanonical* Hamiltonian mechanics [38, 39], where condition (3.7) is obsolete, becomes necessary in the guiding center formalism.

Hamilton's equations in canonical formalism read

$$\dot{\bar{\mathbf{q}}} = \frac{\partial H}{\partial \bar{\mathbf{p}}} \quad \text{and} \quad \dot{\bar{\mathbf{p}}} = -\frac{\partial H}{\partial \bar{\mathbf{q}}}, \tag{3.8}$$

where $H(\bar{\mathbf{q}}, \bar{\mathbf{p}})$ stands for *Hamiltonian*. Our quest is to find similar equations for an arbitrary choice of coordinates. We begin by defining the *phase space Lagrangian*

$$\mathcal{L}(\bar{\mathbf{q}}, \dot{\bar{\mathbf{q}}}, \bar{\mathbf{p}}, \dot{\bar{\mathbf{p}}}) \equiv \bar{\mathbf{p}} \cdot \dot{\bar{\mathbf{q}}} - H(\bar{\mathbf{q}}, \bar{\mathbf{p}}), \tag{3.9}$$

which is just the ordinary Lagrangian expressed in coordinates $(\bar{\mathbf{q}}, \bar{\mathbf{p}}, \dot{\bar{\mathbf{q}}}, \dot{\bar{\mathbf{p}}})$. These coordinates are similar to the usual $(\bar{\mathbf{q}}, \dot{\bar{\mathbf{q}}})$ coordinates used in Lagrangian mechanics, and one can confirm that substituting $\mathcal{L}(\bar{\mathbf{q}}, \bar{\mathbf{p}}, \dot{\bar{\mathbf{q}}}, \dot{\bar{\mathbf{p}}})$ to *Euler-Lagrange equation*,

$$\frac{d}{dt}\left(\frac{\partial L}{\partial \dot{\bar{\mathbf{x}}}}\right) = \frac{\partial L}{\partial \bar{\mathbf{x}}}, \qquad \bar{\mathbf{x}} \in \{\bar{\mathbf{q}}, \bar{\mathbf{p}}\}, \tag{3.10}$$

indeed leads to Hamilton's equations (3.8). Our motivation behind the definition (3.9) was to separate variables $\bar{\mathbf{q}}$ and $\bar{\mathbf{p}}$, and their respective derivatives so that we are free to make coordinate transformation to *general coordinates* $\bar{\mathbf{z}}$. Adopting Einstein summation notation, the derivatives in terms of the new coordinates are

$$\dot{\bar{\mathbf{q}}} = \dot{\bar{z}}^\alpha \frac{\partial \bar{\mathbf{q}}}{\partial \bar{z}^\alpha}. \tag{3.11}$$

Thus, the phase space Lagrangian (3.9) in general coordinates reads

$$\mathcal{L}(\bar{\mathbf{z}}) = \lambda_\alpha \dot{\bar{z}}^\alpha - H(\bar{\mathbf{z}}), \tag{3.12}$$

where

$$\lambda_\alpha \equiv \bar{\mathbf{p}} \cdot \frac{\partial \bar{\mathbf{q}}}{\partial \bar{z}^\alpha} \tag{3.13}$$

is the *sympletic* part of the Lagrangian.

The Lagrangian in general phase space coordinates now enables us to employ the Euler-Lagrange equation to obtain the equations of motion we

were looking for. Substituting the Lagrangian (3.12) to the Euler-Lagrange equation (3.10) yields

$$\tilde{\omega}_{\alpha\beta}\dot{\bar{z}}^{\beta} = \frac{\partial H}{\partial \bar{z}^{\alpha}}, \tag{3.14}$$

where $\tilde{\boldsymbol{\omega}}$ is the so-called *Lagrange matrix*

$$\tilde{\omega}_{\alpha\beta} \equiv \frac{\partial \lambda_{\beta}}{\partial \bar{z}^{\alpha}} - \frac{\partial \lambda_{\alpha}}{\partial \bar{z}^{\beta}}. \tag{3.15}$$

Assuming that $\tilde{\boldsymbol{\omega}}$ is invertible, the inverse being known as the *Poisson matrix*, $\boldsymbol{\Pi} \equiv \tilde{\boldsymbol{\omega}}^{-1}$, Eq. (3.14) leads to equations of motion

$$\dot{\bar{z}}^{\alpha} = \Pi^{\alpha\beta}\frac{\partial H}{\partial \bar{z}^{\beta}}, \tag{3.16}$$

which are now expressed in general (noncanonical) coordinates as desired.

Anticipating the guiding center transform of the equations of motion, it would be beneficial if we could express Eq. (3.16) with a single operator. If it is possible, then we would just need to find the expression in the guiding center coordinates for this operator only. It turns out that it can be accomplished by defining the *Poisson bracket* for arbitrary functions f and g as

$$\{f, g\} \equiv \frac{\partial f}{\partial \bar{z}^{\alpha}}\Pi^{\alpha\beta}\frac{\partial g}{\partial \bar{z}^{\beta}}, \tag{3.17}$$

which we can use to turn the noncanonical equations of motion (3.16) to a more compact form

$$\dot{\bar{z}}^{\alpha} = \{\bar{z}^{\alpha}, H\}. \tag{3.18}$$

The Poisson bracket also has an alternative form which follows from the conservation of the phase space flow. The conservation law, i.e., the widely known *Liouville theorem*, states

$$\frac{\partial}{\partial \bar{z}^{\alpha}}\left(\mathcal{J}\dot{\bar{z}}^{\alpha}\right) = 0, \tag{3.19}$$

where $\mathcal{J} = \det\tilde{\omega}$ is the *Jacobian* associated with the coordinate transformation. As our system is Hamiltonian, Eq. (3.19) is satisfied, and one can deduce that this leads to the *Liouville identities*

$$\frac{\partial}{\partial \bar{z}^{\alpha}}(\mathcal{J}\Pi^{\alpha\beta}) = 0. \tag{3.20}$$

With these identities, Poisson bracket can be written in a divergence form

$$\{f, g\} = \frac{1}{\mathcal{J}}\frac{\partial}{\partial \bar{z}^{\alpha}}\left(\mathcal{J}f\Pi^{\alpha\beta}\frac{\partial g}{\partial \bar{z}^{\beta}}\right). \tag{3.21}$$

3.3 Guiding center transformation operator

Finding a coordinate system suitable to represent the guiding center phase space was only just the step on the path leading to the guiding center formalism. To capitalize on that, we must find the guiding center equations of motion which turns out to be a complicated task as we are no longer interested in the exact location of the particle but the position of its guiding center. A simple coordinate transformation $\mathbf{X} = \mathbf{x} - \tilde{\boldsymbol{\rho}}$ will not do as the resulting equations of motion would still depend on the gyroangle θ, i.e., the fast oscillation would persist. We approach this problem by treating the fast cyclotron motion as a perturbation, i.e., we write Eq. (3.5) as

$$\mathbf{x} = \mathbf{X} + \epsilon\tilde{\boldsymbol{\rho}}, \tag{3.22}$$

where ϵ is an artificial dimensionless *ordering parameter* that will be set to unity in the end. The ordering parameter can be introduced by renormalizing the particle charge $q \to \epsilon^{-1}q$ since the gyroradius $\tilde{\rho} \sim q^{-1}$. Performing a near-identity transformation up to the desired order results in guiding center Lagrangian and Hamiltonian of the corresponding order. With the guiding center Lagrangian, guiding center Poisson bracket can be constructed and the equations of motion obtained with Eq. (3.18).

By demanding that the transformed Lagrangian and Hamiltonian are gyrophase independent, we ensure that the resulting equations of motion describe the guiding center motion only. This requirement can be met with the use of the *Lie transform* [34]

$$\mathbf{Z} = \exp\left(\epsilon\mathcal{L}_{\mathbf{G}}\right)\mathbf{z}, \tag{3.23}$$

where $\mathcal{L}_{\mathbf{G}}$ is a *Lie derivative* along the vector field $\mathbf{G}$. Here, $\mathbf{z}$ denote the particle phase space coordinates and $\mathbf{Z}$ the guiding center coordinates. It is possible to choose $\mathbf{G}$ in a way that the transformation achieves the gyrophase independency although it cannot be managed with just a single transformation. Therefore, the guiding center transformation is obtained by performing successive Lie transforms

$$\mathbf{Z} = \exp\left(\epsilon\mathcal{L}_{\mathbf{G}_1}\right)\exp\left(\epsilon^2\mathcal{L}_{\mathbf{G}_2}\right)\exp\left(\epsilon^3\mathcal{L}_{\mathbf{G}_3}\right)\cdots\mathbf{z}, \tag{3.24}$$

where the order of the transformation can be controlled with ϵ. Usually, guiding center transformation is performed to the first order, which already involves the magnetic field nonuniformity, but second order transformation has also been employed [40].

Expanding exponentials with Taylor series, one obtains, up to the second order,

$$\mathbf{Z} = \left[1 + \epsilon\mathcal{L}_{\mathbf{G}_1} + \epsilon^2\left(\mathcal{L}_{\mathbf{G}_2} + \frac{1}{2}\mathcal{L}^2_{\mathbf{G}_1}\right) + \dots\right]\mathbf{z} \equiv \mathcal{T}_{gc}\mathbf{z}, \tag{3.25}$$

where $\mathcal{T}_{gc} : \mathbf{z} \to \mathbf{Z}$ is the Lie transform *pull-back* operator. Inverse transform $\mathcal{T}^{-1}_{gc} : \mathbf{Z} \to \mathbf{z}$, that is, the *push-forward* operator, is correspondingly

$$\mathbf{z} = \exp\left(-\epsilon\mathcal{L}_{\mathbf{G}_1}\right)\exp\left(-\epsilon^2\mathcal{L}_{\mathbf{G}_2}\right)\exp\left(-\epsilon^3\mathcal{L}_{\mathbf{G}_3}\right)\cdots\mathbf{Z}, \tag{3.26}$$

whose series expansion is

$$\mathbf{z} = \left[1 - \epsilon\mathcal{L}_{\mathbf{G}_1} - \epsilon^2\left(\mathcal{L}_{\mathbf{G}_2} - \frac{1}{2}\mathcal{L}^2_{\mathbf{G}_1}\right) + \dots\right]\mathbf{Z} \equiv \mathcal{T}^{-1}_{gc}\mathbf{Z}. \tag{3.27}$$

Comparing Eqs. (3.22) and (3.25), one can obtain an intuitive understanding of the guiding center Lie transform. The transformation moves the initial position along vector field $\mathbf{G}_n$ by a distance ϵ^n: in spatial coordinates, this corresponds to moving along gyrovector $\tilde{\boldsymbol{\rho}}$ from $\mathbf{x}$ to $\mathbf{X}$.

For illustration purposes, we will now give an example of Lie transformation of an arbitrary tensor $\boldsymbol{\gamma}$. Assuming that we know the vector fields $\mathbf{G}_n$ generating the Lie transforms, we can transform a tensor $\boldsymbol{\gamma}$, represented as a power series

$$\boldsymbol{\gamma} = \boldsymbol{\gamma}_0 + \epsilon\boldsymbol{\gamma}_1 + \epsilon^2\boldsymbol{\gamma}_2 + \dots, \tag{3.28}$$

to the new set of coordinates via push-forward operator (3.27). The transformed tensor is

$$\boldsymbol{\Gamma} = \boldsymbol{\Gamma}_0 + \epsilon\boldsymbol{\Gamma}_1 + \epsilon^2\boldsymbol{\Gamma}_2 + \dots, \tag{3.29}$$

where

$$\boldsymbol{\Gamma}_0 = \boldsymbol{\gamma}_0, \tag{3.30}$$

$$\boldsymbol{\Gamma}_1 = \boldsymbol{\gamma}_1 - \mathcal{L}_{\mathbf{G}_1}\boldsymbol{\gamma}_0, \tag{3.31}$$

$$\boldsymbol{\Gamma}_2 = \boldsymbol{\gamma}_2 - \mathcal{L}_{\mathbf{G}_1}\boldsymbol{\gamma}_1 - \left(\frac{1}{2}\mathcal{L}^2_{\mathbf{G}_1} - \mathcal{L}_{\mathbf{G}_2}\right)\boldsymbol{\gamma}_0, \tag{3.32}$$

and so on. Operator L acting on a scalar function f is transformed to the guiding center phase space as

$$\mathcal{T}^{-1}_{gc}(Lf)(\mathbf{z}) = (\mathcal{T}^{-1}_{gc}L)f(\mathbf{z}) = (L_{gc}F)(\mathbf{Z}), \tag{3.33}$$

where $L_{gc} = \mathcal{T}^{-1}_{gc}L$ and $F(\mathbf{Z}) = f(\mathbf{z})$ is the scalar function f in the guiding center coordinates. More information about Lie transform pertubation theory, and how to define vector fields $\mathbf{G}_n$ in the guiding center transformation can be found at Refs. [34, 36].

3.4 Non-Hamiltonian motion due to collisions

Our treatment of the guiding center motion so far applies only if interactions with other particles are ignored. In a plasma, interparticle interactions are complicated as the test particle interacts with every particle inside its Debye sphere at the same time. Therefore, to evaluate the interactions, we resort to kinetic plasma theory, where the microscopic details are averaged out. As the kinetic theory describes the behavior of the particle population as a whole, we shift our focus from one test particle to the plasma distribution function for the time being. Theorems found in this section are explained more thoroughly in Refs. [3, 36, 41], and here only the main points are presented.

Time evolution of the distribution function of one particle species f is given by the *Vlasov-Boltzmann equation*

$$\frac{\partial f}{\partial t} + \dot{z}^\alpha \frac{\partial f}{\partial z^\alpha} = C[f], \tag{3.34}$$

which forms the basis of the kinetic description of a plasma. The term $\dot{z}^\alpha$ contains the Hamiltonian motion arising from the macroscopic electromagnetic fields, whereas collision term C accounts for the microscopic fields that particles experience from the unscreened charges found inside their Debye spheres. Assuming that most collisions result in small scattering angles (which holds for the fusion relevant plasmas), the collision operator takes the form

$$C[f] = -\frac{\partial}{\partial z^\alpha}\left(K^\alpha f - \frac{\partial}{\partial z^\beta}(D^{\alpha\beta} f)\right), \tag{3.35}$$

where

$$\mathbf{K} \equiv \frac{\langle \Delta \mathbf{z} \rangle}{\tau_{coll}}, \tag{3.36}$$

$$\mathbf{D} \equiv \frac{\langle \Delta \mathbf{z} \Delta \mathbf{z} \rangle}{\tau_{coll}}. \tag{3.37}$$

For simplicity, we have assumed here that z^α is expressed in cartesian coordinates. Equation (3.35) is known as the *Fokker-Planck collision operator*, and the coefficients (3.36) and (3.37) correspondingly as the *Fokker-Planck coefficients*. $\langle \Delta \mathbf{z} \rangle$ refers to average change in particle phase space coordinates due to a single collision with τ_{coll} being the timescale associated with the collisions. Collisions in plasma are regarded as point-like Coulomb collisions only affecting particle momentum, i.e., $\Delta \mathbf{z} \to \Delta \mathbf{p}$.

Substituting the Fokker-Planck form for the collision operator (3.35) to the Vlasov-Boltzmann equation (3.34), and using the Liouville theorem (3.19), yields the *Fokker-Planck equation*

$$\frac{\partial f}{\partial t} = -\frac{\partial}{\partial z^\alpha}[(\dot{z}^\alpha + K^\alpha)f] + \frac{\partial^2}{\partial z^\alpha \partial z^\beta}[D^{\alpha\beta} f]. \tag{3.38}$$

The Fokker-Planck equation is closely related to a stochastic differential equation known as the *Langevin equation*

$$d\mathbf{z} = \mathbf{A}dt + \boldsymbol{\sigma} \cdot d\mathcal{W}, \tag{3.39}$$

where $\mathcal{W}$ is the *standard Wiener process*. The theorem connecting these two equations states that whenever motion of each particle in a population is governed by the Langevin equation, the time-evolution of the associated distribution function obeys the Fokker-Planck equation (3.38). The coefficients in these two equations are related to each other as

$$\mathbf{A} = \dot{\mathbf{z}} + \mathbf{K} \quad \text{and} \quad \mathbf{D} = \frac{1}{2}\boldsymbol{\sigma}\boldsymbol{\sigma}^T. \tag{3.40}$$

We can now return to the single particle picture knowing that the equation of motion is given in the form of the Langevin equation (3.39) once the Fokker-Planck coefficients (3.36) and (3.37) are known. Assuming isotropic plasma, the coefficients take the form

$$\mathbf{K} = -K(p)\mathbf{p}, \tag{3.41}$$

$$\mathbf{D} = D_\parallel(p)\frac{\mathbf{pp}}{p^2} + D_\perp(p)\left(\mathbf{I} - \frac{\mathbf{pp}}{p^2}\right), \tag{3.42}$$

where especially the latter is useful result as a diagonal matrix is straightforward to decompose as (3.40). The Fokker-Planck equation (3.38) in particle phase space $(\mathbf{x}, \mathbf{p})$ now reads

$$\frac{\partial f}{\partial t} = -\frac{\partial}{\partial x^i}\left[\dot{x}^i f\right] - \frac{\partial}{\partial p^i}\left[(\dot{p}^i + K^i)f\right] + \frac{\partial^2}{\partial p^i \partial p^j}\left[D^{ij} f\right], \tag{3.43}$$

where index i counts for the three spatial components in real space. Equation (3.43) leads to corresponding equations of motion for a single particle

$$d\mathbf{x} = \dot{\mathbf{x}}dt, \tag{3.44}$$

$$d\mathbf{p} = (\dot{\mathbf{p}} - K(p)\mathbf{p})\,dt + \left(\sqrt{2D_\parallel(p)}\frac{\mathbf{pp}}{p^2} + \sqrt{2D_\perp(p)}\left(\mathbf{I} - \frac{\mathbf{pp}}{p^2}\right)\right) \cdot d\mathcal{W}^{\mathbf{p}}. \tag{3.45}$$

Coefficients **K** and **D** are also called *friction* and *diffusion* coefficients respectively. The reason is clear from above: **K** decreases the magnitude of the momentum but does not change its direction, whereas **D** also causes scattering which leads the particle population to diffuse.

To include the collisions in the guiding center formalism, we need to transfer the Fokker-Planck equation to the guiding center phase space. First, we cast Eq. (3.43) as

$$\frac{\partial f}{\partial t} = -\frac{\partial}{\partial x^i}\left[\dot{x}^i f\right] - \frac{\partial}{\partial p^i}\left[(\dot{p}^i + \kappa^i) f\right] + \frac{\partial}{\partial p^i}\left[D^{ij}\frac{\partial}{\partial p^j} f\right], \tag{3.46}$$

where we have notated

$$\boldsymbol{\kappa} = \mathbf{K} - \frac{\partial}{\partial \mathbf{p}} \cdot \mathbf{D}. \tag{3.47}$$

Now, we need to use the property of the particle phase space Poisson bracket which allows expressing the momentum gradient of an arbitrary function g as

$$\frac{\partial g}{\partial \mathbf{p}} = \{\mathbf{x}, g\}. \tag{3.48}$$

This formula is easily deduced when we later present the explicit form for the particle Poisson bracket. With Eq. (3.48), the particle phase space Fokker-Planck equation (3.46) transforms into

$$\frac{\partial f}{\partial t} + \{f, H\} = \{x^i, \kappa^i f - D^{ij}\{x^j, f\}\}. \tag{3.49}$$

Now, the Poisson brackets can be transformed to the guiding center coordinates via transformation rule (3.33) which results in

$$\begin{aligned} \frac{\partial F}{\partial t} + \{F, H_{gc}\}_{gc} &= \{\mathcal{T}_{gc}^{-1} x^i, (\mathcal{T}_{gc}^{-1}\kappa^i)F - (\mathcal{T}_{gc}^{-1} D^{ij})\{\mathcal{T}_{gc}^{-1} x^j, F\}_{gc}\}_{gc} \\ &\equiv C_{gc}[F], \end{aligned} \tag{3.50}$$

where F is the distribution function f in the guiding center phase space.

Equation (3.50) is not yet suitable for evaluating collisions in the guiding center picture as the distribution function F depends on the gyroangle θ. Eliminating this dependence begins with decomposing the distribution function as as

$$F = \frac{1}{2\pi}\int_0^{2\pi} F d\theta + \tilde{F} \equiv \langle F \rangle + \tilde{F}, \tag{3.51}$$

where $\langle F \rangle$ is the gyroaveraged F and $\tilde{F}$ contains the residual of this operation. Gyroaverage over Eq. (3.50) together with Eq. (3.51) results in a pair

of equations

$$\frac{\partial \langle F\rangle}{\partial t} + \{\langle F\rangle, H_{gc}\}_{gc} = \langle C_{gc}[F]\rangle = \langle C_{gc}[\langle F\rangle]\rangle + \left\langle C_{gc}[\tilde{F}]\right\rangle, \tag{3.52}$$

$$\frac{\partial \tilde{F}}{\partial t} + \{\tilde{F}, H_{gc}\}_{gc} = C_{gc}[F] - \langle C_{gc}[F]\rangle. \tag{3.53}$$

The coupling term $\left\langle C_{gc}[\tilde{F}]\right\rangle$ in Eq. (3.52) can be ignored when the particle motion is dominated by the Hamiltonian motion and not by the collisions. This condition is satisfied in all situations where the guiding center approximation itself is valid so we can proceed to treat the gyroaveraged equation (3.52) alone, which now reads

$$\frac{\partial \langle F\rangle}{\partial t} + \{\langle F\rangle, H_{gc}\}_{gc} = \langle C_{gc}[\langle F\rangle]\rangle. \tag{3.54}$$

To use the theorem connecting the Fokker-Planck equation with the Langevin equation, Eq. (3.54) must be expressed first in a similar form as Eq. (3.38). Replacing Poisson brackets with their divergence form (3.21), results in

$$\frac{\partial \langle F\rangle}{\partial t} + \frac{1}{\mathcal{J}}\frac{\partial}{\partial Z^\alpha}(\mathcal{J}\dot{Z}^\alpha \langle F\rangle) = -\frac{1}{\mathcal{J}}\frac{\partial}{\partial Z^\alpha}\left[\mathcal{J}\left(\kappa^\alpha_{gc}\langle F\rangle - D^{\alpha\beta}_{gc}\frac{\partial \langle F\rangle}{\partial Z^\beta}\right)\right], \tag{3.55}$$

where the guiding center Fokker-Planck coefficients

$$\kappa^\alpha_{gc} = \left\langle (\mathcal{T}^{-1}_{gc}\boldsymbol{\kappa})\cdot \boldsymbol{\Delta}^\alpha\right\rangle, \tag{3.56}$$

$$D^{\alpha\beta}_{gc} = \left\langle (\boldsymbol{\Delta}^\alpha)^\dagger \cdot (\mathcal{T}^{-1}_{gc}\mathbf{D})\cdot \boldsymbol{\Delta}^\beta\right\rangle, \tag{3.57}$$

are defined in terms of the projection vectors

$$\boldsymbol{\Delta}^\alpha \equiv \{\mathcal{T}^{-1}_{gc}\mathbf{x}, Z^\alpha\}. \tag{3.58}$$

Now, we can cast Eq. (3.55) as

$$\begin{aligned}\frac{\partial \langle F\rangle}{\partial t} =& -\frac{1}{\mathcal{J}}\frac{\partial}{\partial Z^\alpha}\left[\mathcal{J}\left(\dot{Z}^\alpha + \kappa^\alpha_{gc} + \frac{1}{\mathcal{J}}\frac{\partial}{\partial Z^\beta}(\mathcal{J}D^{\alpha\beta}_{gc})\right)\langle F\rangle\right] \\ &+ \frac{\partial^2}{\partial Z^\alpha \partial Z^\beta}\left[\mathcal{J}D^{\alpha\beta}_{gc}\langle F\rangle\right],\end{aligned} \tag{3.59}$$

which is in a similar form as Eq. (3.38). Hence, we obtain the Langevin equation for a guiding center

$$dZ^\alpha = A^\alpha_{gc}dt + \sigma^{\alpha\beta}_{gc}d\mathcal{W}^\beta, \tag{3.60}$$

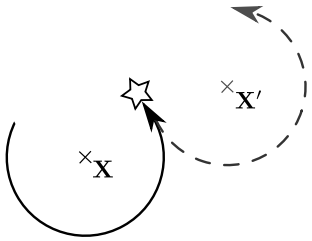

Figure 3.2: Illustration of the displacement of the particle guiding center due to collision. Here, for the purpose of a clear visualization, the particle changes its direction to the opposite direction after the collision. Collisions in a plasma typically result in small scattering angles.

where the first coefficient is

$$A^{\alpha}_{gc} = \dot{Z}^{\alpha} + \kappa^{\alpha}_{gc} + \frac{1}{\mathcal{J}} \frac{\partial}{\partial Z^{\beta}} (\mathcal{J} D^{\alpha\beta}_{gc}), \tag{3.61}$$

and the second one is defined by the relation

$$D^{\alpha\beta}_{gc} = \frac{1}{2} \sigma^{\alpha\gamma}_{gc} \sigma^{\beta\gamma}_{gc}. \tag{3.62}$$

The guiding center Fokker-Planck coefficients can be transformed to other coordinate system according to the relation

$$\kappa^{\alpha}_{gc} = \kappa^{\gamma}_{gc} \frac{\partial Z^{\alpha}}{\partial Z^{\gamma}} \quad \text{and} \quad D^{\alpha\beta}_{gc} = \frac{\partial Z^{\alpha}}{\partial Z^{\gamma}} D^{\gamma\delta}_{gc} \frac{\partial Z^{\beta}}{\partial Z^{\delta}}, \tag{3.63}$$

which follow from the properties of the Poisson bracket. Therefore, the coefficients need to be evaluated only once from Eqs. (3.56) and (3.57), after which other coordinate representations are found with Eq. (3.63).

One should note that even though Fokker-Planck coefficients in particle picture had nonzero components only in the momentum space, the same does not apply in the guiding center formalism. Presence of the guiding center spatial coordinate $\mathbf{X}$ in Eq. (3.58) implies that collisions affect also the spatial coordinates of the guiding center. This is exactly the result one would expect as the guiding centers are not physical particles, but the centers of the gyromotion. For example, considering a particle that experiences a collision which causes its parallel momentum to change its sign. This causes the particle to gyrate in the opposing direction thus creating a sudden jump of the guiding center position as depicted in Fig. 3.2. Therefore, the guiding center spatial collision coefficients describe the classical diffusion.

In closing remarks, we note that the original Vlasov equation only included the test particle species. However, the results we obtained can be expanded to include interactions with other particle species by replacing the collision term with a sum over all particle species

$$C[f] \rightarrow \Sigma_b C_{ab}[f_a], \tag{3.64}$$

where a refers to the test particle species and C_{ab} is the collision operator between species a and b. Thus, the results we obtained in this section remain valid when we require that Fokker-Planck coefficients are summed over all particle species.

Chapter 4

Relativistic test particle in a magnetized plasma

Whether a physical system should be considered relativistic or not, is determined by the *Lorentz factor*,

$$\gamma = \frac{mc^2 + \mathcal{E}_{kin}}{mc^2}, \tag{4.1}$$

which is the ratio of particle energy to its rest mass. Alternatively, it can also be defined as $\gamma \equiv 1/\sqrt{1 - v^2/c^2}$. Here c is the speed of light in vacuum while v is the relative velocity between inertial reference frames, for example, the particle speed measured in the lab frame. As special relativity is an extension of the classical mechanics, the classical results are obtained when one replaces Lorentz factor with its first order Taylor expansion $\gamma \approx 1 + \frac{1}{2}\frac{v^2}{c^2}$.

Ions in fusion plasmas are rarely relativistic as even the 3.5 MeV alpha particles born in D-T fusion have $\gamma = 1.001$. On the other hand, modern fusion plasmas routinely reach a temperature of over 10 keV where thermal velocity of an electron exceeds $5.8 \cdot 10^7$ m/s, corresponding to $\gamma = 1.02$. Nonetheless, these thermal electrons may be considered at most weakly relativistic. Runaway electrons are the only truly relativistic species in fusion plasmas: with the energy of 1 MeV they have $\gamma = 3.0$, and a physicist using only the classical mechanics would fail miserably when trying to understand their behavior.

This chapter focuses on laying the theoretical basis for the motion of a relativistic particle in a plasma. This basis is employed later on when numerical schemes for the particle tracing are implemented. As these schemes usually make use of the guiding center formalism, behavior of both the particle and the guiding center is examined. The main results presented in this chapter are collected from Refs. [3, 37, 42–44].

4.1 Equations of motion in a static electromagnetic field

Particle motion is governed by the *Lorentz force* when the particle is charged and moving through an electromagnetic field. The *Lorentz force law*

$$\mathbf{F} = q\left(\mathbf{E} + \mathbf{v} \times \mathbf{B}\right), \tag{4.2}$$

where m and q are the particle mass and charge, respectively, is already compatible with the special relativity. Thus we could end our treatment of the particle motion here and use Eq. (4.2) with Newtonian mechanics (accounting for relativity) to obtain the equations of motion. However, we need the particle Lagrangian if we are to use the Lie perturbation theory (section 3.3) to come up with the guiding center dynamics. Therefore, we use this opportunity to employ methods presented in section 3.2 to derive the particle equations of motion. Here we follow the derivation found in Ref. [42].

Defining charged particle Hamiltonian as

$$H \equiv \gamma mc^2 + q\Phi, \tag{4.3}$$

where Φ is the electric potential associated with the electric field $\mathbf{E}$, leads to Lagrangian

$$L = \left(\mathbf{p} + \epsilon^{-1} q\mathbf{A}\right) \cdot \dot{\mathbf{x}} - H, \tag{4.4}$$

with $\mathbf{A}$ being the magnetic vector potential associated with the magnetic field $\mathbf{B}$. Anticipating the guiding center transformation, we have already introduced the ordering parameter ϵ in Eq. (4.4) but, for now, it can be ignored. The equation (4.4) assumes electromagnetic fields are static, an assumption commonly made in particle following codes. With the Lagrangian, we can calculate the corresponding Lagrange matrix (3.15) and invert that to get the Poisson matrix, thus acquiring the particle Poisson bracket from Eq. (3.17):

$$\{f, g\} = \frac{\partial f}{\partial \mathbf{x}} \cdot \frac{\partial g}{\partial \mathbf{p}} - \frac{\partial f}{\partial \mathbf{p}} \cdot \frac{\partial g}{\partial \mathbf{x}} + q\mathbf{B} \cdot \frac{\partial f}{\partial \mathbf{p}} \times \frac{\partial g}{\partial \mathbf{p}}. \tag{4.5}$$

One can now confirm that the formula

$$\frac{\partial g}{\partial \mathbf{p}} = \{\mathbf{x}, g\}, \tag{4.6}$$

we applied in section 3.4, holds.

With the particle Poisson bracket (4.5) and formula (3.16), one can derive the equations of motion, arriving at

$$\dot{\mathbf{x}} = \{\mathbf{x}, H\} = \frac{1}{\gamma m}\mathbf{p}, \tag{4.7}$$

$$\dot{\mathbf{p}} = \{\mathbf{p}, H\} = q\left(\mathbf{E} + \frac{1}{\gamma m}\mathbf{p} \times \mathbf{B}\right). \tag{4.8}$$

One can now assure the validity of this method by noting that the change in momentum is due to the Lorentz force as expected.

With the particle motion taken care of, we proceed to search for the corresponding equations for the guiding center motion. First, we transfer the particle Hamiltonian (4.3) and Lagrangian (4.4) to the guiding center phase space $(\mathbf{X}, p_\parallel, \mu, \theta)$ via Lie transform perturbation methods introduced in section 3.3. The vector field generating the Lie derivatives is chosen as to make H and L independent of the gyroangle, thus detaching the fast gyromotion from the guiding center motion. The resulting Hamiltonian is the same as in the particle formalism [34]

$$H_{gc} \equiv \gamma mc^2 + q\Phi, \tag{4.9}$$

and the Lagrangian becomes

$$L_{gc} = \left(\epsilon^{-1} q\mathbf{A} + p_\parallel \hat{\mathbf{b}}\right) \cdot \dot{\mathbf{X}} + \epsilon \frac{\mu m}{q}\dot{\theta} - H_{gc}, \tag{4.10}$$

where the Lorentz factor in the guiding center phase space can be evaluated as $\gamma = \sqrt{1 + (2/mc^2)\mu B + p_\parallel^2/(mc)^2}$. One should be advised that the fields are now evaluated at the guiding center location instead of the exact particle location. The guiding center Poisson bracket is

$$\begin{aligned}\{f, g\}_{gc} =& \epsilon^{-1}\frac{q}{m}\left(\frac{\partial f}{\partial \theta}\frac{\partial g}{\partial \mu} - \frac{\partial f}{\partial \mu}\frac{\partial g}{\partial \theta}\right) \\ &+ \frac{\mathbf{B}^*}{B_\parallel^*} \cdot \left(\frac{\partial f}{\partial \mathbf{X}}\frac{\partial g}{\partial p_\parallel} - \frac{\partial f}{\partial p_\parallel}\frac{\partial g}{\partial \mathbf{X}}\right) \\ &- \epsilon\frac{\hat{\mathbf{b}}}{qB_\parallel^*} \cdot \frac{\partial f}{\partial \mathbf{X}} \times \frac{\partial g}{\partial \mathbf{X}},\end{aligned} \tag{4.11}$$

where the effective fields are

$$\mathbf{B}^* \equiv \mathbf{B} + \epsilon(p_\parallel/q)\nabla \times \hat{\mathbf{b}}, \tag{4.12}$$

$$\mathbf{E}^* \equiv \mathbf{E} - \epsilon(\mu/\gamma q)\nabla B, \tag{4.13}$$

and $B_\parallel^* = \mathbf{B}^* \cdot \hat{\mathbf{b}}$. The Jacobian related to these coordinates is $\mathcal{J} = mB_\parallel^*$.

Once again, calculating the equations of motion with noncanonical Hamiltonian mechanics is a trivial exercise after the corresponding Poisson bracket and Hamiltonian have been found. The resulting equations are [42]

$$\dot{\mathbf{X}} = \{\mathbf{X}, H_{gc}\}_{gc} = \frac{p_\parallel}{\gamma m}\frac{\mathbf{B}^*}{B_\parallel^*} + \mathbf{E}^* \times \frac{\hat{\mathbf{b}}}{B_\parallel^*}, \tag{4.14}$$

$$\dot{p}_\parallel = \{p_\parallel, H_{gc}\}_{gc} = q\mathbf{E}^* \cdot \frac{\mathbf{B}^*}{B_\parallel^*}, \tag{4.15}$$

$$\dot{\mu} = \{\mu, H_{gc}\}_{gc} = 0, \tag{4.16}$$

$$\dot{\theta} = \{\xi, H_{gc}\}_{gc} = \epsilon^{-1}\Omega, \tag{4.17}$$

where *gyrofrequency* $\Omega = qB/\gamma m$. As desired, our result is independent of the gyroangle θ. One may validate these equations by extracting the familiar guiding center drifts, e.g. grad-B drift, from them. We now see that the ordering parameter makes a clear separation of time scales associated with the particle motion: terms of order ϵ^{-1} corresponds to cyclotron motion, the zeroth order is the intermediate motion parallel to the magnetic field, and the first order accounts for the slow drifting across the field. The ordering parameter was introduced by renormalizing the particle charge $q \to \epsilon^{-1}q$ and one may have wondered why ϵ was not present in the term involving the electric potential in the particle Hamiltonian (4.3). Working through the calculations, one finds that this term produces the well-known $E \times B$ drift. This drift is usually comparable to the parallel motion in magnitude, so we implicitly renormalized also the electric potential $\Phi \to \epsilon\Phi$ in order to have $E \times B$ drift as a zeroth order term.

4.2 Abraham-Lorentz-Dirac force

An accelerating charged particle emits electromagnetic radiation which causes it to experience a recoil force. When the relativistic effects are accounted for, this reaction force is represented by the *Abraham-Lorentz-Dirac (ALD) force* [45]

$$\mathbf{\Gamma} = \frac{q^2\gamma^2}{6\pi\epsilon_0 c^3}\left[\ddot{\mathbf{v}} + \frac{3\gamma^2}{c^2}(\mathbf{v}\cdot\dot{\mathbf{v}})\dot{\mathbf{v}} + \frac{\gamma^2}{c^2}\left(\mathbf{v}\cdot\ddot{\mathbf{v}} + \frac{3\gamma^2}{c^2}(\mathbf{v}\cdot\dot{\mathbf{v}})^2\right)\mathbf{v}\right]. \tag{4.18}$$

Why was this radiation reaction force not included in the particle Lagrangian? The reason is that we implicitly assumed that the particle does not affect the surrounding electromagnetic field. This assumption was essential as there

exists no Lagrangian formulation outside quantum mechanics that would include the coupling between particles and fields. The assumption effectively excluded radiation losses as these are in essence perturbations to the electromagnetic field.

As it is, Eq. (4.18) can be incorporated directly in the equations of motion of a particle by coupling it with the Lorentz force. However, a more practical formulation for the ALD force can be found by assuming that the cyclotron motion dominates the particle motion, i.e., $\mathbf{v} \cdot \dot{\mathbf{v}} \approx 0$. With this assumption, together with relation

$$\ddot{\mathbf{v}} = -\frac{q^2 B^2}{\gamma^3 m^3} \mathbf{p}_\perp, \tag{4.19}$$

which derives directly from the Lorentz force, Eq. (4.18) becomes

$$\mathbf{\Gamma} \approx -\tau_r^{-1} \left(\mathbf{p}_\perp + \frac{p_\perp^2}{(mc)^2} \mathbf{p} \right). \tag{4.20}$$

Here τ_r is the characteristic time for the radiation reaction force, defined as

$$\tau_r \equiv \frac{q^4 B^2}{6\pi\epsilon_0 \gamma (mc)^3}. \tag{4.21}$$

The characteristic time scale of the cyclotron motion is Ω^{-1}. By comparing these two time scales, we see that $\Omega\tau_r^{-1} \approx 9 \cdot 10^{11}$ [T]$/B$ for electrons which shows that the ALD force has little effect on the particle trajectory on a time scale of the cyclotron motion. Therefore, the Lorentz force dominates over ALD force which validates the assumption $\mathbf{v} \cdot \dot{\mathbf{v}} \approx 0$.

On longer time scales, the recoil force becomes important as it affects the particle energy unlike the $q\mathbf{v} \times \mathbf{B}$ force. The particle energy is affected also by collisions. However, as we will see in the next section, the collision frequency decreases as the particle energy increases. This is in contrast with the ALD force whose magnitude increases as a function of the particle energy. For runaway electrons, the ALD force may dominate the energy losses. One should also note that $\tau_r^{-1} \sim m^{-3}$ so it is unlikely that the ALD force has any significant effect on ions at relevant energies.

To transform the ALD force to the guiding center formalism, we first write the collisionless Vlasov equation in particle phase space as

$$\frac{\partial f}{\partial t} + \frac{\partial}{\partial \mathbf{z}} \cdot \left[(\dot{\mathbf{z}} + \mathbf{\Gamma}) f \right] = 0, \tag{4.22}$$

where we have included $\mathbf{\Gamma}$ as an extra force term. By proceeding in similar manner as in section 3.4, where we transformed the Fokker-Planck coefficients to the guiding center phase space, we obtain the equation of motion

$$d\mathbf{Z} = (\dot{\mathbf{Z}} + \mathbf{\Gamma}_{gc}) dt. \tag{4.23}$$

The change in the guiding center phase space coordinates due to the Lorentz force is contained within $\dot{\mathbf{Z}}$. The guiding center ALD force is

$$\Gamma_{gc}^{\alpha} = \left\langle \mathbf{\Delta}^{\alpha} \cdot \mathcal{T}_{gc}^{-1} \mathbf{\Gamma} \right\rangle, \tag{4.24}$$

where the projection vectors are defined in Eq. (3.58). Evaluating the Eq. (4.24) up to the zeroth order gives [43]

$$\Gamma_{gc}^{p_{\parallel}} = -2\tau_r p_{\parallel} \frac{\mu B}{mc^2}, \tag{4.25}$$

$$\Gamma_{gc}^{\mu} = -2\tau_r \mu \left(1 + \frac{2\mu B}{mc^2}\right). \tag{4.26}$$

If the first order terms, which account for the magnetic field uniformity, were included, there would have been a spatial term $\Gamma_{gc}^{\mathbf{x}}$ also. However, we limit our treatment of the ALD force to the zeroth order because the higher order terms will be insignificant in practise as will be demonstrated later.

4.3 Relativistic Fokker-Planck coefficients

In section 3.4, we discussed on how to incorporate the collisional dynamics in the particle motion. There, we found that when the time evolution of the distribution function of a particle species obeys the Fokker-Planck equation, the collisional dynamics are defined by the Fokker-Planck coefficients. The Fokker-Planck collision operator assumes that collisions are regarded as Coulomb collisions, i.e., small scattering angle collisions affecting only the particle momentum. Additionally, if the plasma is assumed to be locally homogeneous, with constant density n and temperature T, the Fokker-Planck coefficients become

$$\mathbf{K} = \frac{\langle \Delta \mathbf{p} \rangle}{\tau_{coll}}, \tag{4.27}$$

$$\mathbf{D} = \frac{\langle \Delta \mathbf{p} \Delta \mathbf{p} \rangle}{\tau_{coll}}. \tag{4.28}$$

Evaluating these coefficients from the first principles is a tedious task [3, 46] and outside the scope of this work. We can, however, discuss the nature of these coefficients in the nonrelativistic regime where they have simpler forms compared to the relativistic case.

In the nonrelativistic regime, the Fokker-Planck coefficients are [3]

$$\mathbf{K} = \frac{C_{ab}}{n_b}\left(1+\frac{m_a}{m_b}\right)\frac{\partial h_b}{\partial \mathbf{p}}, \tag{4.29}$$

$$\mathbf{D} = \frac{1}{2}\frac{C_{ab}}{n_b}\frac{\partial}{\partial \mathbf{p}}\frac{\partial}{\partial \mathbf{p}} g_b, \tag{4.30}$$

where

$$h_b(\mathbf{v}) = \int d\mathbf{p}' f_b(\mathbf{p}')\frac{1}{|\mathbf{p}-\mathbf{p}'|}, \tag{4.31}$$

$$g_b(\mathbf{v}) = \int d\mathbf{p}' f_b(\mathbf{p}')|\mathbf{p}-\mathbf{p}'|, \tag{4.32}$$

are the *Rosenbluth potentials*, and $C_{ab} \equiv q_a^2 q_b^2 n_b \ln\Lambda/4\pi\epsilon_0^2$ with $\ln\Lambda$ being the *Coulomb logarithm*. Here, we have used the subscripts a and b to refer to the test particle species and background species, respectively.

The Rosenbluth potentials (4.31) and (4.32) depend on the velocity distribution of the particle species. Particle following codes usually operate with equilibrium plasmas where the background plasma is Maxwellian. As one may recall from section 3.4, the Fokker-Planck coefficients can be decomposed as

$$\mathbf{K} = K(p)\hat{\mathbf{p}}, \tag{4.33}$$

$$\mathbf{D} = D_{\parallel}(p)\hat{\mathbf{p}}\hat{\mathbf{p}} + D_{\perp}(p)\left(\mathbf{I}-\hat{\mathbf{p}}\hat{\mathbf{p}}\right), \tag{4.34}$$

when the background is isotropic. If the background plasma can be further assumed to be Maxwellian and nonrelativistic, the coefficients become

$$K = -\frac{C_{ab}}{v_b}\left(1+\frac{m_a}{m_b}\right)\left(\frac{v}{v_b}\right)G(v/v_b), \tag{4.35}$$

$$D_{\parallel} = \frac{C_{ab}}{2}G(v/v_b), \tag{4.36}$$

$$D_{\perp} = \frac{C_{ab}}{2}\left(\mathrm{erf}(v/v_b) - \frac{1}{2}G(v/v_b)\right), \tag{4.37}$$

where $v_b \equiv \sqrt{2T_b/m_b}$ is the background thermal velocity, $\mathrm{erf}(x)$ is the *error function*, and

$$G(x) = \frac{\mathrm{erf}(x) - \frac{2x}{\sqrt{\pi}}\exp(-x^2)}{x^2}. \tag{4.38}$$

Furthermore, one can also evaluate Eq. (3.47) to obtain

$$\boldsymbol{\kappa} = -\frac{C_{ab}}{v_b^2}\frac{m_a}{m_b}G(v/v_b)\hat{\mathbf{v}}, \tag{4.39}$$

which is needed if one wishes to find the guiding center collision operator in the nonrelativistic case.

Extending to the relativistic regime (both the plasma and and the test particle can be relativistic), the Rosenbluth potentials are replaced by their relativistic counterparts: the *Karney potentials* [47]. Furthermore, Maxwell-Boltzmann distribution for relativistic species is

$$f_b(\gamma) = \frac{\gamma^2 v e^{-\gamma/\Theta_b}}{c\Theta_b K_2(1/\Theta_b)}, \tag{4.40}$$

where K_2 is the 2nd order *modified Bessel function of the second kind*, and $\Theta_b \equiv T_b/m_b c^2$. The relativistic Maxwell-Boltzmann distribution, also known as *Maxwell-Jüttner* distribution, ensures no particle travels faster than the speed of light as Fig. 4.1 illustrates. With these alterations, the Fokker-Planck coefficients become [44]

$$K = -\frac{C_{ab}}{u^2}\left(\frac{1}{\gamma m_a}\mu_0 + \frac{1}{m_b}\mu_1\right), \tag{4.41}$$

$$D_\parallel = \frac{C_{ab}\gamma c^2}{u^3}\Theta_b \mu_1, \tag{4.42}$$

$$D_\perp = \frac{C_{ab}c^2}{2\gamma u^3}\left[\frac{u^2}{c^2}(\mu_0 + \gamma\Theta_b\mu_1') - \Theta_b\mu_1\right], \tag{4.43}$$

where the special functions μ_0, μ_1, and μ_1' are defined as

$$\mu_0(u,\Theta_b) = \frac{\gamma^2 L_0 - \Theta_b L_1 + (\Theta_b - \gamma)ue^{-\gamma/\Theta_b}}{K_2(1/\Theta_b)c}, \tag{4.44}$$

$$\mu_1(u,\Theta_b) = \frac{\gamma^2 L_1 - \Theta_b L_0 + (\Theta_b\gamma - 1)ue^{-\gamma/\Theta_b}}{K_2(1/\Theta_b)c}, \tag{4.45}$$

$$\mu_1'(u,\Theta_b) \equiv \frac{\partial\mu_1}{\partial\gamma} = \frac{2\Theta_b\gamma L_1 + (1+2\Theta_b^2)ue^{-\gamma/\Theta_b}}{\Theta_b K_2(1/\Theta_b)c}, \tag{4.46}$$

with L_0 and L_1 being

$$L_0 = \int_0^u \frac{e^{-\gamma(u')/\Theta_b}}{\gamma(u')}du', \quad L_1 = \int_0^u e^{-\gamma(u')/\Theta_b}du'. \tag{4.47}$$

The Fokker-Planck coefficients are now functions of normalized momentum $u \equiv p/m_a$ instead of v. The Lorentz factor expressed with u is $\sqrt{1+u^2/c^2}$. One can confirm that in the limit $u \to v$ and $\Theta_b \ll 1$, the coefficients (4.41)-(4.43) reduce to their nonrelativistic counterparts (4.35)-(4.37).

From now on, transforming the Fokker-Planck coefficients is just a matter of algebra since we have already derived the transformation rule and the

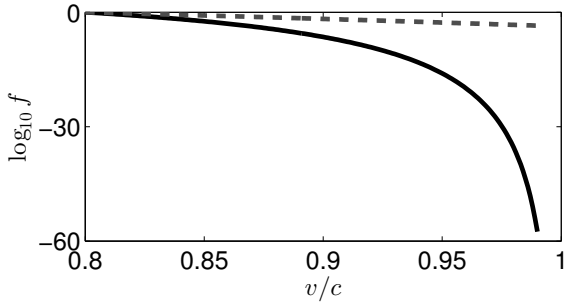

Figure 4.1: Illustration of how Maxwell-Boltzmann distribution behaves close to the speed of light depending whether relativistic effects are included (solid line) or not (dashed).

guiding center Poisson bracket is known. However, performing the calculations becomes increasingly more complicated when aiming for higher order terms. Therefore, we restrict ourselves to the zeroth order, meaning that magnetic non-uniformities are not accounted for. We first need to substitute the relativistic Fokker-Planck coefficients into Eq. (3.47) which results in

$$\kappa = -\frac{C_{ab}}{m_b u^2}\mu_1. \tag{4.48}$$

Evaluating Eqs. (3.56) and (3.57) gives the guiding center transformations [37]

$$\kappa_{gc}^{p_\parallel} = \kappa \tag{4.49}$$

$$D_{gc}^{\mu\mu} = \frac{2\mu}{m_a B}\left[(D_\parallel - D_\perp)\frac{\mu B}{\mathcal{E}} + D_\perp\right] \tag{4.50}$$

$$D_{gc}^{p_\parallel p\parallel} = D_\parallel + \left(D_\perp - D_\parallel\right)\frac{\mu B}{\mathcal{E}} \tag{4.51}$$

$$D_{gc}^{\mu p\parallel} = \left(D_\parallel - D_\perp\right)\frac{\mu p_\parallel}{\mathcal{E}}, \tag{4.52}$$

where $\mathcal{E}$ is the particle kinetic energy. Furthermore, we have

$$D_{gc}^{\mathbf{xx}} = \left[\left(D_\parallel - D_\perp\right)\frac{\mu B}{2\mathcal{E}} + D_\perp\right]\frac{\mathbf{I} - \hat{\mathbf{b}}\hat{\mathbf{b}}}{(m\Omega)^2} \tag{4.53}$$

with all other components of $\mathbf{K}_{gc}$ and $\mathbf{D}_{gc}$ being zero. As mentioned, coordinates $(\mathbf{X}, p, \xi, \theta)$ are more useful when treating collisions, so we apply

rule (3.63) to obtain

$$\kappa_{gc}^{p} = \kappa \tag{4.54}$$

$$D_{gc}^{pp} = D_{\parallel}, \tag{4.55}$$

$$D_{gc}^{\xi\xi} = (1-\xi^2)\frac{D_{\perp}}{p^2}, \tag{4.56}$$

where the guiding center diffusion coefficient is diagonalized. We now possess the relativistic guiding center Fokker-Planck coefficients and are ready to apply these in the next chapter where we implement relativistic collisions to ASCOT.

Chapter 5

Implementing relativistic effects to ASCOT

ASCOT [18] is an orbit following code designed for studying fast ions such as alpha particles and beam ions [48, 49]. Nevertheless, it is in principle capable of simulating other plasma species also, as long as that species is in minority. The simulated species cannot play a significant role in the total plasma behavior in short timescales since ASCOT functions in static background only. Furthermore, interactions between test particles are omitted, so by itself, ASCOT cannot investigate nonlinear phenomena. The runaway electrons form a minority species so they present a suitable candidate for ASCOT simulations.

The core of ASCOT is the *particle following* in which the particle motion is integrated over time. The particle trajectory can be traced exactly in the *full orbit* (FO) mode [50], or one can choose to follow its *guiding center* (GC) which is more computationally effective as we have argued. In both cases, the time integration of the Hamiltonian motion, from now on referred as *orbit following*, and the collisions, i.e. the *collisional part* of the equation of motion, are separated. In GC mode, the orbit following and collisional part both have their own integration timesteps which are independent of one another. The particle following proceeds by doing the orbit following first for a specific time interval, and the collisional part is integrated afterwards for a same amount of time. The time interval is chosen so that collisions are taken frequently enough, and it has usually a length of one to five orbit following timesteps, and it is at maximum of one collisional part timestep. In FO mode, the orbit following and collisional part have different integrators but they use same timestep.

There are two reasons for separating the collisions from the orbit following. Firstly, orbit following must be performed with high accuracy so

that numerical drift in energy does not grow too large in longer simulations. This calls for implementing the orbit following with high-order integration methods so that the integration timestep does not have to be impractically small. Unfortunately, there are no feasible higher-order methods for stochastic equations, so the collisional part cannot be integrated together with the orbit following. Secondly, integration timestep for orbit integrator is chosen so that specific boundary limits are fulfilled. These boundary limits for example define how far the particle can travel in the toroidal direction. The timestep depends on the particle state via boundary limits. Therefore, having the orbit and the collision integrator use the same timesteps would bias the stochastic part of the equation of motion as the stochastic process must be independent of the particle state. This bias is weak in FO mode as there the timestep varies only a little. Therefore, different timesteps for orbit following and collisional part need not to be used.

This chapter describes the implementation and provides verification for the new features that ASCOT has to have in order to carry out RE simulations, namely the ALD force and the relativistic Fokker-Planck collision operator. Since ALD is a deterministic effect, it is implemented with the orbit following. Relativistic equations of motion themselves were already implemented, so these are only verified. All new features are implemented for both FO and GC modes.

5.1 Orbit following and ALD force

Orbit following in ASCOT in both FO and GC methods employs fourth order Runge-Kutta method with fifth order error estimation, that is, the *Cash-Karp method* [51]. In this method, the timestep is determined at each step by the pre-defined error tolerance. In the FO mode, ASCOT features also an option to use *Leap-Frog method*. Unlike Runge-Kutta method, the Leap-Frog method does not cause numerical drift in particle energy, which is a desirable feature in long simulations. However, although a Leap-Frog scheme already exists for the relativistic equations of motion [52], it cannot be employed as it is when the ALD force is present. Evaluating Hamiltonian motion with Leap-Frog method, and including ALD force with some other integration scheme is possible. However, it was not done in this work since the actual simulations in this thesis will be done in GC mode, and FO mode is only used for benchmarking the GC mode.

The relativistic equations of motion for both the particle and the guiding center were already implemented in ASCOT. These equations were completed with the addition of the ALD force. Written explicitly, the resulting equations

in FO mode are

$$\dot{\mathbf{x}} = \frac{1}{\gamma m}\mathbf{p}, \tag{5.1}$$

$$\dot{\mathbf{p}} = q\left(\mathbf{E} + \frac{1}{\gamma m}\mathbf{p}\times\mathbf{B}\right) - \tau_r\left(\mathbf{p}_\perp + \frac{p_\perp^2}{(mc)^2}\mathbf{p}\right). \tag{5.2}$$

For a guiding center, the corresponding equations are

$$\dot{\mathbf{X}} = \frac{p_\parallel}{\gamma m}\frac{\mathbf{B}^*}{B_\parallel^*} + \mathbf{E}^*\times\frac{\hat{\mathbf{b}}}{B_\parallel^*}, \tag{5.3}$$

$$\dot{p}_\parallel = q\mathbf{E}^*\cdot\frac{\mathbf{B}^*}{B_\parallel^*} - 2\tau_r p_\parallel\frac{\mu B}{mc^2}, \tag{5.4}$$

$$\dot{\mu} = -2\tau_r\mu\left(1 + \frac{2\mu B}{mc^2}\right), \tag{5.5}$$

$$\dot{\theta} = \Omega, \tag{5.6}$$

with

$$\mathbf{B}^* \equiv \mathbf{B} + (p_\parallel/q)\nabla\times\hat{\mathbf{b}}, \tag{5.7}$$

$$\mathbf{E}^* \equiv \mathbf{E} - (\mu/\gamma q)\nabla B. \tag{5.8}$$

To verify these equations and their implementation, a test particle, an electron with the energy of 1 MeV and pitch of 0.9, was placed in a 2D ITER magnetic field and traced with ASCOT. These tests excluded collisions as those are treated separately later. In the first tests, also the ALD force was disabled. This enabled the inspection of the numerical drift in energy as, physically, the energy should be conserved in this case. The particle was traced for 1 ms to make drifts in energy evident. The drifts for different modes and Cash-Karp error tolerances are shown in Fig. 5.1a. Which error tolerance should be used depends on the required accuracy as well as on the limits set by the computational resources. In this thesis, we value accuracy over simulation time, the simulations being relatively inexpensive computationally, and use a value of 1e-10 for both FO and GC modes. One should note that the energy conservation of FO mode is still quite poor. The next test, Fig. 5.1b, verified that the more complicated guiding center equations of motion are correctly implemented by comparing them to the simple FO equations. These simulations, where the particle was traced for 0.1 ms, also included parallel electric field so that the particle energy can be compared as well. The agreement between FO and GC modes is evident in Fig. 5.1b. Finally, the ALD force was enabled which resulted in energy losses shown

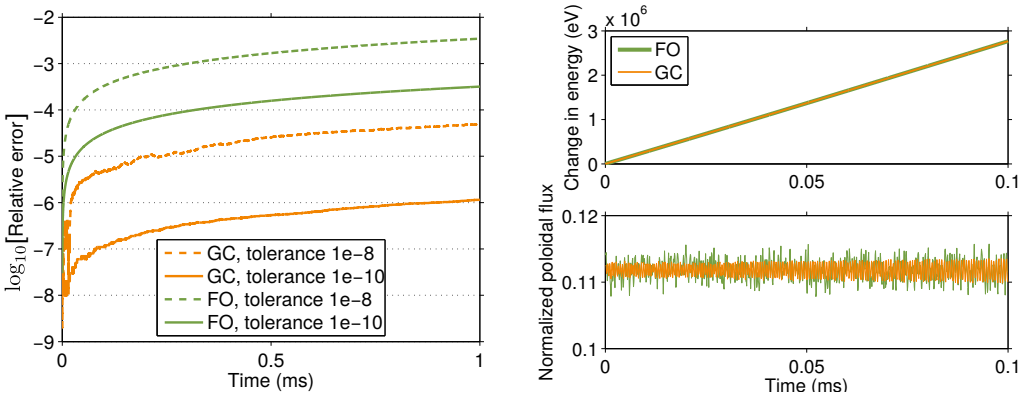

(a) (b)

Figure 5.1: Verification of ASCOT orbit following in the relativistic regime. (a) Global truncation error in particle energy in FO and GC modes with different local truncation error tolerances. The y-axis is in $\log_{10}$ scale. (b) Particle energy and location in presence of the parallel electric field $E = 100$ V/m. The particle state was not recorded at each timestep which causes the oscillations seen in FO location. The orbit widening is due to the increased particle energy.

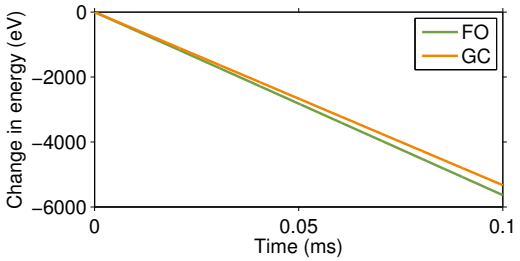

Figure 5.2: Energy loss due to ALD in FO and GC modes.

in Fig. 5.2. Accounting for the numerical energy drift in FO mode, it seems that implementing only the zeroth order terms for ALD force is sufficient in practice.

5.2 Collisions

Before the collisional part of the equation of motion can be integrated, the Fokker-Planck coefficients need to be evaluated. The evaluation of the non-relativistic Fokker-Planck coefficients was already implemented in ASCOT. For this work, these were replaced with the ones that are valid also at rela-

tivistic speeds. However, the new coefficients contain special functions, recall Eqs. (4.44)-(4.46), that need to be calculated numerically. More explicitly, the integrals (4.47) and the function $K_2(1/\Theta_b)$ cannot be expressed analytically. The function $K_2(x)$ is the second-order modified Bessel function of the second kind, for which the implementation to ASCOT is straight-forward when taking advantage of the existing numerical libraries. The open-source libraries provide tools for computing the zeroth and the first order modified Bessel functions of the second kind [53], and these can be used to obtain values for higher order functions via recursive relation

$$K_{n+1}(x) = K_{n-1}(x) - \frac{2n}{x} K_n(x), \tag{5.9}$$

which holds for all $n > 1$.

The integrals (4.47), however, are not as common and the reviewed open-source libraries did not contain an effective method for computing them. Even though the integrals are one-dimensional, numerical evaluation is difficult due to the variable Θ_b. Θ_b depends on the temperature and mass of the background species, so it has a wide range: electrons at $T = 10$ keV have $\Theta_b \approx 10^{-2}$, while protons at $T = 1$ eV have $\Theta_b \approx 10^{-9}$, for example. As Θ_b is present in the exponent, its smallness causes the integrals to have extremely small values which can induce floating point errors when implemented in a code. Fortunately, the exponential term is present also in the terms not involving the integrals. Thus, we can cast the functions (4.44)-(4.46) in the form

$$\mu_0(u, \Theta_b) = \frac{\gamma^2 L_0^* - \Theta_b L_1^* + (\Theta_b - \gamma) u e^{(1-\gamma)/\Theta_b}}{K_2^* c}, \tag{5.10}$$

$$\mu_1(u, \Theta_b) = \frac{\gamma^2 L_1^* - \Theta_b L_0^* + (\Theta_b \gamma - 1) u e^{(1-\gamma)}}{K_2^* c}, \tag{5.11}$$

$$\mu_1'(u, \Theta_b) = \frac{2\Theta_b \gamma L_1^* + (1 + 2\Theta_b^2) u e^{(1-\gamma)}}{\Theta_b K_2^* c}, \tag{5.12}$$

where

$$K_2^* \equiv K_2(1/\Theta_b) e^{1/\Theta_b}, \tag{5.13}$$

$$L_0^* \equiv \int_0^u \frac{e^{(1-\gamma(u'))/\Theta_b}}{\gamma'} du', \tag{5.14}$$

$$L_1^* \equiv \int_0^u e^{(1-\gamma(u'))/\Theta_b} du', \tag{5.15}$$

without affecting the values of μ_0, μ_1, and μ_1'. Now the scale factor e^{1/Θ_b} in each term ensures that the values given by the integrals stay within a reasonable range.

The other issue is that, given small Θ_b, the integrand in Eqs. (5.14) and (5.15) decays rapidly in u' and, therefore, most contribution comes from near the origin. Evaluating these integrals by standard methods that divide the integration interval into n intervals of equal length requires large n for an accurate result. The number of computations grows with n, so the standard approach is not useful here. Instead, we first note that both integrands equal to unity at $u = 0$. As the integrands decay rapidly, the integrals have practically constant values beyond a certain point. Therefore, we introduce the *cut-off point*, u_{cutoff}, defined from relation

$$e^{(1-\gamma_{cutoff})/\Theta_b} = \varepsilon \qquad \Rightarrow \qquad u_{cutoff} = c\sqrt{(1 - \Theta \ln \varepsilon)^2 - 1}, \tag{5.16}$$

where ε is the value of the exponential term at u_{cutoff}. Computing the integrals (5.14) and (5.15) over an interval $[0, u_{cutoff}]$ with, e.g., Simpsons rule, an accurate result is obtained efficiently with the suitable choice of parameter ε.

Now that the obstacles in evaluating the functions have been overcome, the relativistic Fokker-Planck coefficients, Eqs. (4.41) (4.43), can be computed. With these, we can proceed to evaluate the collisional part of the equation of motion by utilizing the *Euler-Maruyama method* [54]. In FO mode, the discretized equation of motion reads

$$\Delta \mathbf{p} = A\Delta t \hat{\mathbf{p}} + \sigma_{\parallel}\Delta t^{1/2}(\boldsymbol{\beta} \cdot \hat{\mathbf{p}})\hat{\mathbf{p}} + \sigma_{\perp}\Delta t^{1/2}[\boldsymbol{\beta} - (\boldsymbol{\beta} \cdot \hat{\mathbf{p}})\hat{\mathbf{p}}], \tag{5.17}$$

where

$$A = \kappa, \tag{5.18}$$

$$\sigma_{\parallel} = \sqrt{2D_{\parallel}}, \tag{5.19}$$

$$\sigma_{\perp} = \sqrt{2D_{\perp}}, \tag{5.20}$$

are calculated from the Fokker-Planck coefficients. Here $\boldsymbol{\beta}$ is a random vector variable, each component of which has to be an independent random variable with $\mathrm{E}[\beta_i] = 0$ and $\mathrm{Var}[\beta_i] = 1$. These conditions are fulfilled if we use the binary distribution for generating the random variables, i.e, the random variables are assigned either a value of -1 or $+1$ from a uniform distribution.

In GC mode, the corresponding equations of motion are

$$\Delta \mathcal{E} = A_{\mathcal{E}}\Delta t + \beta_{\mathcal{E}}\sigma_{\mathcal{E}}\Delta t^{1/2}, \tag{5.21}$$

$$\Delta \xi = -\nu\xi\Delta t + \beta_{\xi}\sqrt{(1 - \xi^2)\nu\Delta t}, \tag{5.22}$$

$$\Delta \mathbf{X} = \sigma_{\mathbf{X}}(\mathbf{I} - \hat{\mathbf{b}}\hat{\mathbf{b}}). \tag{5.23}$$

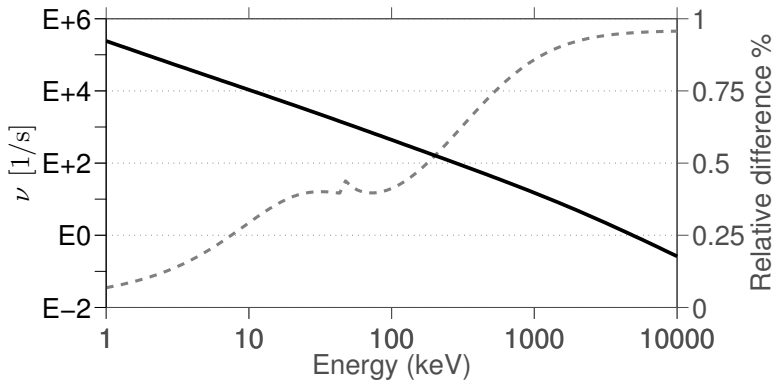

Figure 5.3: Relativistic pitch collision frequency (solid black line) of an electron with different energies. Grey dashed curve is the relative difference between the relativistic and the nonrelativistic case defined as $(\nu_{\text{relativistic}} - \nu_{\text{classical}})/\nu_{\text{relativistic}}$.

Here, the coefficients $A_{\mathcal{E}}$, $\sigma_{\mathcal{E}}$, ν, and $D^{\mathbf{X}}$ are

$$A_{\mathcal{E}} = \left(\kappa + 2D_{\parallel} + \frac{\partial D_{\parallel}}{\partial p}\right)\frac{p}{\gamma m}, \tag{5.24}$$

$$\sigma_{\mathcal{E}} = \sqrt{2D_{\parallel}}\frac{p}{\gamma m}, \tag{5.25}$$

$$\nu = \frac{2D_{\parallel}}{p^2}, \tag{5.26}$$

$$\sigma_{\mathbf{X}} = \frac{1}{m\Omega}\sqrt{\left(D_{\parallel} - D_{\perp}\right)\frac{\mu B}{2\mathcal{E}} + D_{\perp}}, \tag{5.27}$$

where

$$\frac{\partial D_{\parallel}}{\partial p} = \frac{C_{ab}\Theta_b}{mu^3}\left(u\mu_1' - \frac{3c^2 + 2u^2}{\gamma u}\mu_1\right). \tag{5.28}$$

With the collision operator implemented, we can make a comparison between the relativistic and nonrelativistic collision coefficients. Figures 5.3 and 5.4 show this comparison for coefficients calculated in a deuterium plasma with a temperature and density of 10 keV and 10^{20} m^{-3}, respectively. In the nonrelativistic limit, the coefficients agree well, and even at high energies the difference is not large. The peak in Fig. 5.3 at 100 keV seems like an artifact but it turns out it is indeed a similar peak as in Fig. 5.4a but using a logarithmic scale.

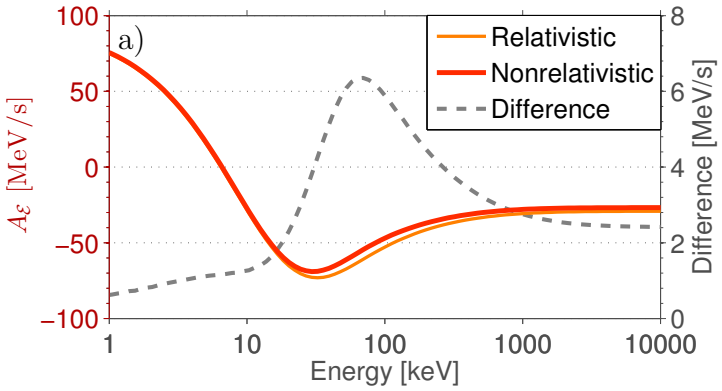

(a)

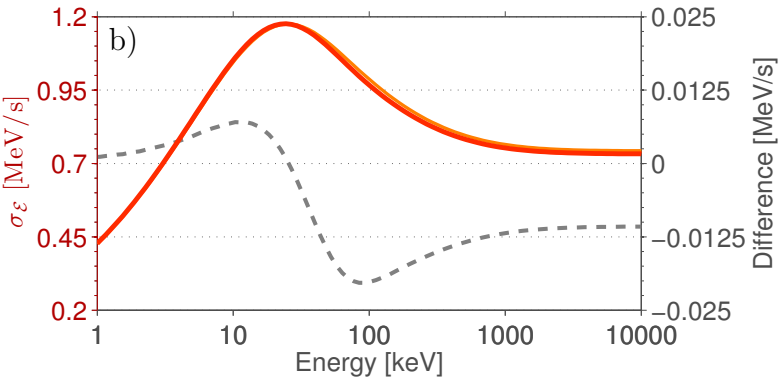

(b)

Figure 5.4: Coefficients of the energy collision operator for an electron at different energies: Fig. (a) shows the deterministic part, and Fig. (b) the stochastic part. Grey dashed curve is the difference between the relativistic and the nonrelativistic case.

Chapter 6

Radial transport in a perturbed magnetic field

Having extended ASCOT to a relativistic regime, we now turn our attention to the problem of runaway electron (RE) transport in a perturbed magnetic field. The transport is a combination of stochastic transport due to field structure, orbit widening as electric field accelerates the particle, and collisional transport. From these, the field structure dominates the transport but it remains poorly understood as discussed in chapter 2. In order to focus on the field-induced transport, we, somewhat ironically, omit the ALD force and collisions from the investigations done in this chapter. Electric field is also omitted and we can assume the particles have a constant energy. With these simplifications the transport becomes time independent. Future work should include these effects we neglect here to gain a full understanding of the RE transport.

Figure 6.1a shows the structure of the magnetic field used as a testbed for our transport studies. The field is a ITER vacuum field with unmitigated toroidal ripple that is perturbed with ELM coils to create a stochastic region to the edge [48]. The methods used to compute the unperturbed field are described in Ref. [55]. The radial coordinate we have used here, ρ_{pol}, is defined according to $\rho_{\mathrm{pol}} = \sqrt{(\psi - \psi_{\mathrm{axis}})/(\psi_{\mathrm{sep}} - \psi_{\mathrm{axis}})}$, where ψ_{axis} and ψ_{sep} are poloidal fluxes at the magnetic axis and separatrix, respectively. The fluxes are evaluated from an axisymmetric equilibrium. Starting from the edge, the field is fully stochastic until, at $\rho_{\mathrm{pol}} \approx 0.85$, magnetic islands begin to form at specific toroidal positions. Magnetic islands, which are formed when magnetic flux tubes close upon themselves, have a significant effect on transport since particles caught there are confined as will be demonstrated later. The $n = 3$ islands grow in size when moving deeper into plasma, and additional smaller islands appear, until island chain with clearly identifiable

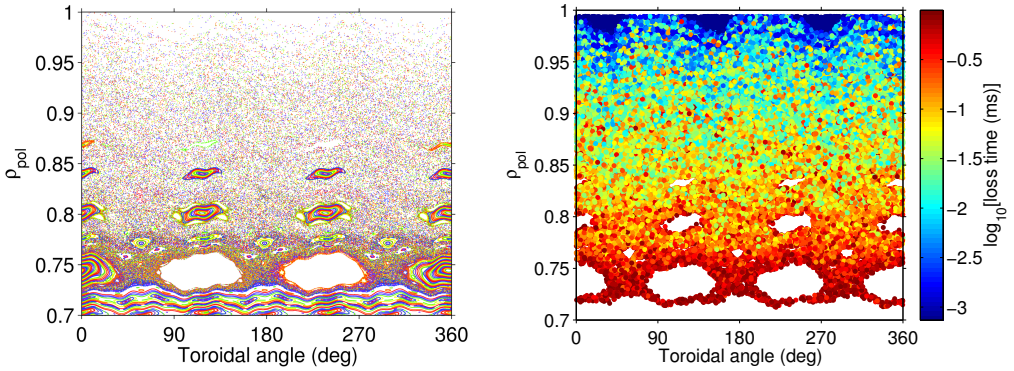

(a) (b)

Figure 6.1: Illustration of the magnetic field where the transport is studied. (a) Poincaré plot of the field recorded at the outer midplane. Colors serve to separate between individual field lines. (b) RE transport associated this field. Color indicates the time it took for a RE starting from the given position (at outer midplane) to be lost. Confined particles are shown in white.

O- and X-points are encountered at $\rho_{\mathrm{pol}} \approx 0.75$. The X-points show peculiar field structure as they are formed by field lines exhibiting a stochastic behavior. This stochastic region at $\rho_{\mathrm{pol}} \approx 0.75$ appears to be significantly more *dense* than the outer region at $\rho_{\mathrm{pol}} \approx 0.8$. Therefore, one can expect there to be a 'threshold' where the magnitude of the transport is changed rapidly as transport is most likely lower where the stochastic field is more dense in nature. Finally, confined field lines are found at $\rho_{\mathrm{pol}} \approx 0.7$, inside which there is no particle transport.

One should take note that the above discussion about the relation between particle transport and field structure is only valid if we assume that particles follow field lines faithfully. Of course, this is not the case since particle deviates from its original trajectory due to the guiding center drifts which are proportional to particle momentum. This picture becomes even more complicated if particles are trapped poloidally. Since REs mostly have pitch close to unity, we are going to exclude trapped particles from this discussion.

In order to see how REs are transported in the field shown in Fig. 6.1a, we initialize RE population with $\mathcal{E} = 10$ MeV and $\xi = 0.9$ in the region ranging from $\rho_{\mathrm{pol}} = 0.7$ to $\rho_{\mathrm{pol}} = 1.0$, and simulate it with ASCOT. The exact energy and pitch distribution of REs in ITER is unknown but the chosen values represent a reasonable estimate. Test particles are initialized at the outer midplane, for reasons discussed later, and each particle is given a random toroidal and radial location from a uniform distribution. The particles are

simulated for 1 ms, and the time it takes for a particle to be lost, dubbed *loss time*, is recorded. Particles that are not lost during this time are considered confined. A total of 1×10^5 test particles were initialized and simulated, and the results are shown in Fig. 6.1b where particle initial location is colored according to its loss time. By looking at the edge region, $\rho_{\text{pol}} > 0.95$, first, we see that there is a strong toroidal dependence in loss time. In the blue region particles are lost before they can complete even a single poloidal orbit, i.e., they are first orbit losses. This region will grow when particle energy is increased. One should note that if the blue region fills the entire flux surface, particles born there are lost almost immediately and one cannot identify any meaningful transport. Moving away from the edge, the blue regions disappear, and the transport seems to be overall similar, independent of the toroidal angle. The loss time appears to strongly depend on the initial position, which is what one would expect from a transport in a stochastic field. When moving further towards the core, the toroidal average of the loss time seems to increase until the 'threshold', at $\rho_{\text{pol}} = 0.75$, is encountered. Inside the threshold, no particle has escaped within 0.1 ms. Thus, the chaotic variation in loss time, which is present in outer regions, is absent inside the threshold. This reinforces our expectations that the transport is significantly lower in the region where the stochastic field is denser. Furthermore, we expected to see particles born in magnetic islands to be confined, which is also confirmed by comparing island locations in Fig. 6.1a to white regions in Fig. 6.1b. Finally, the beginning of the confined region seems to be at the same location for both field lines and particles.

6.1 The transport model

Our goal is to develop a transport model for collisionless radial transport in 3D magnetic field. The effect of the complex field structure is reduced to transport coefficients that depend on one (radial) coordinate. We choose our radial coordinate to be the same that ASCOT uses, i.e., ρ_{pol} introduced earlier. The coefficients also naturally depend on energy and pitch, since these determine how closely a given RE follows its initial field line. However, before any model can be built, we must make an assumption about the nature of the underlaying transport. Reicester-Rosenbluth diffusion, recall Eq. (2.1), suggests the transport is diffusive, but a recent study claims to refute this [15]. Here we assume the transport is a combination of drift and diffusion. Whether or not this model is invalid, some insight in the transport process will nonetheless be gained.

The drift-diffusion transport is described by a Fokker-Planck equation,

$$\frac{\partial \tilde{n}(\rho_{\mathrm{pol}}, t)}{\partial t} = -\frac{\partial}{\partial \rho_{\mathrm{pol}}}\left(\tilde{K}(\rho_{\mathrm{pol}})\tilde{n}(\rho_{\mathrm{pol}}, t)\right) + \frac{\partial^2}{\partial \rho_{\mathrm{pol}}^2}\left(\tilde{D}(\rho_{\mathrm{pol}})\tilde{n}(\rho_{\mathrm{pol}}, t)\right), \quad (6.1)$$

similar to what we encountered in chapter 3. Here, the *drift and diffusion coefficients*, $\tilde{K}$ and $\tilde{D}$, are defined as

$$\tilde{K} \equiv \lim_{t\to 0} \frac{\langle \Delta \rho_{\mathrm{pol}} \rangle}{t}, \quad (6.2)$$

$$\tilde{D} \equiv \lim_{t\to 0} \frac{\langle \Delta \rho_{\mathrm{pol}}^2 \rangle}{t}, \quad (6.3)$$

$$(6.4)$$

and $\tilde{n}$ is the RE density. The brackets denote the average over the population at a given ρ_{pol}. Since particles that contact the wall are lost, we set an *absorbing boundary condition*, $\tilde{n} = 0$, to $\rho_{\mathrm{pol}} = 1.01$, just outside the separatrix. Likewise, a *reflecting boundary condition*, $\partial\tilde{n}/\partial\rho_{\mathrm{pol}} = 0$, is set on a surface where the confined region begins. The model we have constructed so far applies only to transported particles. In order to account for the whole RE population, we set the total RE number density as $n_{\mathrm{tot}}(\rho_{\mathrm{pol}}, t) \equiv n_{\mathrm{c}}(\rho_{\mathrm{pol}}) + \tilde{n}(\rho_{\mathrm{pol}}, t)$, where n_{c} is the density of confined REs. As $\partial n_{\mathrm{c}}/\partial t = 0$ by definition, the time evolution of n_{tot} is given by Eq. (6.1) together with the boundary conditions. From now on, we refer to this model as *1D-model*.

Since the coefficients have a spatial dependence, solving Eq. (6.1) directly would require using advanced numerical methods such as finite element method. However, we can take advantage of the corresponding Langevin equation,

$$\frac{\partial \rho_{\mathrm{pol}}}{\partial t} = \tilde{K}(\rho_{\mathrm{pol}})dt + \sqrt{2\tilde{D}(\rho_{\mathrm{pol}})}d\mathcal{W}, \quad (6.5)$$

where $\mathcal{W}$ is the standard Wiener process, to solve Eq. (6.1) via Monte Carlo method. This proceeds in a similar manner as previously described ASCOT simulation: REs with constant pitch and energy are populated uniformly between $\rho_{\mathrm{pol}} = 0.7$ and $\rho_{\mathrm{pol}} = 1.0$ surfaces, and traced for 1 ms. While initializing REs, each test particle has a chance of being born confined. The probability of this happening is given by the *fraction of confined particles*, $f_{\mathrm{CP}}(\rho_{\mathrm{pol}}) \equiv n_{\mathrm{c}}(\rho_{\mathrm{pol}})/n_{\mathrm{tot}}(\rho_{\mathrm{pol}})$, given as an input.

The role of ASCOT is to find $\tilde{K}$, $\tilde{D}$, and f_{CP}. However, we cannot use the coefficients evaluated with ASCOT in the 1D-model, unless a mapping between the 3D and 1D spaces is defined. To be precise, we need only a mapping from 2D to 1D space as the coefficients are toroidally averaged

before given to the 1D-model. A complication arises from the particle's poloidal trajectory as its ρ_{pol} coordinate (and pitch) depend on its poloidal position. A particle in the 1D-model with a specific pitch, energy, and ρ_{pol} then has multiple counterparts in 2D (or 3D) space. In order to have a bijective mapping, we define the radial coordinate of the 1D-model as the ρ_{pol} coordinate particle has when it crosses the outer midplane. This definition has to be kept in mind when evaluating the transport coefficients to avoid any inconsistencies.

6.2 Evaluating transport coefficients

By letting ASCOT trace particles from different flux surfaces, and analysing the resulting radial motion, we can evaluate the transport coefficients for a given energy and pitch. Repeating the process for different values of energy and pitch, we finally obtain $\tilde{K}$ and $\tilde{D}$ at desired location in phase space. The method is similar to the one used in evaluating neoclassical transport numerically [56]. A given number of particles with same values for ρ_{pol}, pitch, and energy are initialized at the outer midplane. The particles are distributed toroidally at equal intervals so that their average transport in ρ_{pol} accounts for 3D effects. The particles are traced for 0.1 ms while recording the particle's state each time it passes outer midplane. By recording the position only at outer midplane we avoid attributing orbit topology for transport while also making sure the mapping between ASCOT and the 1D-model holds. ASCOT simulation provides us with each particle's radial position at a corresponding time which we can use to evaluate the transport coefficients. However, some of the particles will be confined and we need to separate those first. If the field is not axisymmetric, confined particles oscillate in ρ_{pol} which could lead to nonzero transport coefficients even when, in reality, all particles are confined. The 0.1 ms simulation time is required for identifying this oscillation so that confined particles can be separated from those that are not confined, thus giving f_{CP}. After the separation, the drift and diffusion coefficients are evaluated separately for each nonconfined particle, and the mean value, i.e., toroidal average, serves as $\tilde{K}$ and $\tilde{D}$.

The above method was tried out in the test background shown in Fig. 6.1a. Electrons with $\mathcal{E} = 10$ MeV and $\xi = 0.9$ were initialized at 32 distinct ρ_{pol}-surfaces ranging from 0.7 to 1.0, each surface having 360 particles. The resulting coefficients are shown in Fig. 6.2. The interpolation is performed with linear method and the extrapolation is done with constant method. Near the separatrix, some particles were lost before they were able to complete even a single poloidal turn which failed the transport coefficient evaluation method.

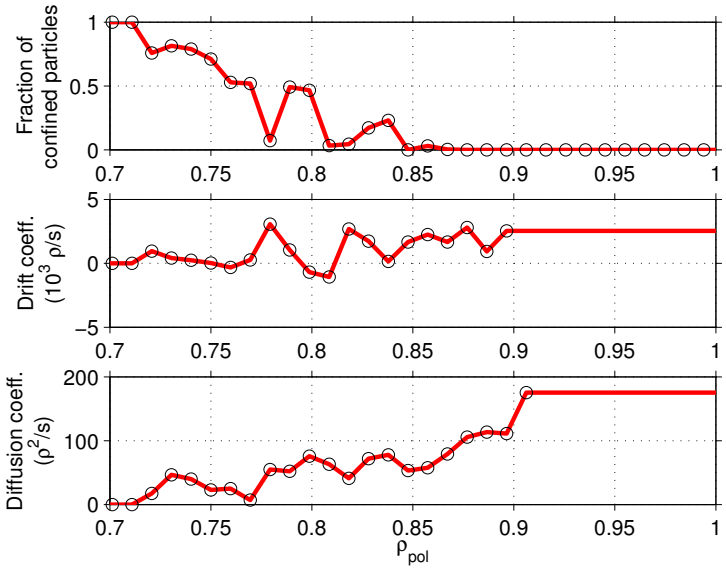

Figure 6.2: Fraction of confined particles together with transport coefficients, all evaluated by tracing REs with ASCOT. RE energy was 10 MeV and pitch 0.9.

The coefficients evaluated there oscillated strongly, were very sensitive to various parameters used in evaluation process, and did not seem to follow the same trend as the coefficients evaluated closer to the core. Therefore, those coefficients were discarded and extrapolated values were used instead.

By comparing f_{CP} in Fig. 6.2 to Figs. 6.1a and 6.1b one can see that there are no confined particles in the region of complete stochasticity. The peaks in f_{CP} correspond to magnetic islands, and the peak height is proportional to the island width at the corresponding flux surface. The majority of the particles are confined inside $\rho_{\mathrm{pol}} \approx 0.75$, a location where we expected to find some sort of threshold behavior in transport. The threshold can be seen in $\tilde{K}$ whose values are close to zero between the threshold and the confined region, but start to grow after the threshold is passed. However, $\tilde{D}$ does not show similar behavior. This is most likely due to the proximity of the boundary of the confined region at $\rho_{\mathrm{pol}} \approx 0.71$. If the particles are reflected from that boundary, the evaluation of the transport coefficients malfunctions which could lead to overestimation of the transport. At $\rho_{\mathrm{pol}} > 0.75$, the increase in $\tilde{D}$ is almost monotonous while $\tilde{K}$ oscillates in a way that seems to correlate with f_{CP}. One should keep in mind that many of the features shown in Fig. 6.2 could be artefacts from the evaluation method whose accuracy is in no way proven. All in all, these results appear to be reasonable but further

testing is warranted.

6.3 Validating transport model

Substituting the results shown in Fig. 6.2 in the 1D-model and carrying out a simulation, we can compare the results given by the 1D-model to those given by the full ASCOT simulation, i.e., those presented in Fig. 6.1b. Figure 6.3a shows how the number of lost particles increases in time according to ASCOT and the 1D-model. The results match well, and also the total number of lost particles is nearly the same in both approaches. Figure 6.3b provides a further comparison by showing the average time during which particles born at a given ρ_{pol} are lost. Once again, the results seem to agree both qualitatively and quantitatively, except inside the threshold region where 1D-model overestimates the transport. However, in that region the number of non-confined particles is so small that this discrepancy is not visible in Fig. 6.3a. Finally, the time evolution of RE density from both approaches are shown in Fig. 6.4. There seem to be only minor differences which probably disappear once the method of evaluating the transport coefficients is developed further. Put together, these results indicate that the transport due to field line stochasticity can be modelled with a simple transport model consisting of drift and diffusion.

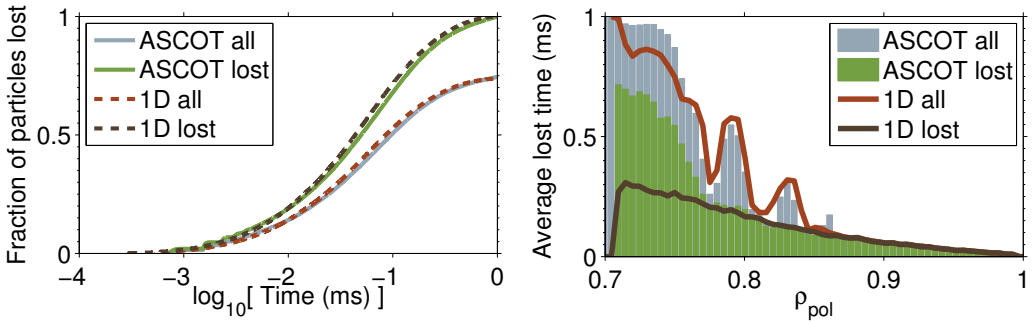

(a) (b)

Figure 6.3: Comparison of RE losses given by ASCOT and the 1D-model when RE energy is 10 MeV and pitch 0.9. (a) Cumulative losses as a function of time. Losses are given either as a fraction of all particles ('all') or as a fraction of total losses ('lost'). (b) The average time within which particles born at a given flux surface are lost. Here 'all' refers to average over all particles, and 'lost' to average over non-confined particles.

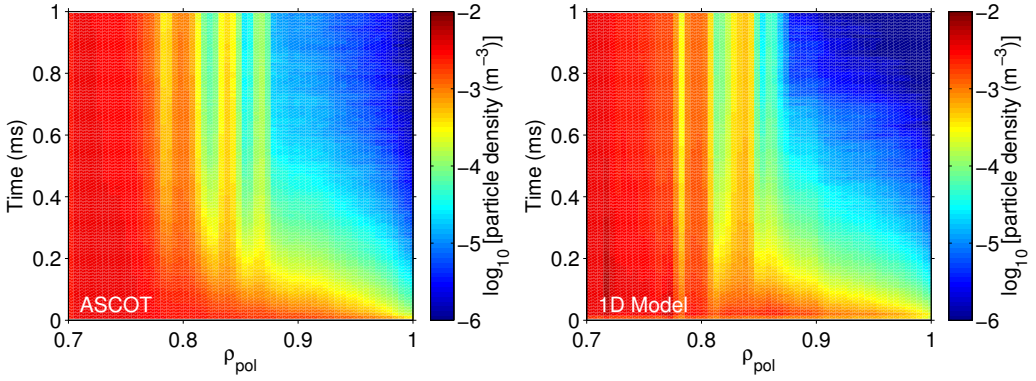

Figure 6.4: Evolution of the RE density in (a) ASCOT and (b) 1D-model. The 'vertical bars' seen in both figures are due to the confined REs whose density stay constant in time.

We replicate the ASCOT simulation described earlier but with different RE populations that have the following parameter pairs: ($\mathcal{E} = 10$ MeV; $\xi = 0.99$), ($\mathcal{E} = 10$ MeV; $\xi = 0.8$), ($\mathcal{E} = 1$ MeV; $\xi = 0.9$), and ($\mathcal{E} = 100$ MeV; $\xi = 0.9$). In other words, we vary energy while keeping pitch constant, and vary pitch while energy is kept constant. The transport coefficients corresponding to each population are evaluated and fed to the 1D-model to further test its validity. The obtained transport coefficients are shown in Fig. 6.5, and the corresponding ASCOT results along with the results given by 1D-model are presented in Figs. 6.6 and 6.7.

As indicated by Fig. 6.5, the value of $\tilde{D}$ is slightly lower when pitch has a lower value. One can confirm the decrease in pitch indeed leads to increased loss times, see Fig. 6.6. However, the transport is qualitatively similar independent of pitch, and there are no large differences in the fraction of confined particles. Therefore, we can deduce that pitch only affects the magnitude of the transport, at least as long as passing particles are concerned. Furthermore, the results show that $\tilde{D}(\xi = 0.8)/\tilde{D}(\xi = 0.99) \approx 0.8/0.99$, i.e., $\tilde{D}$ is directly proportional to pitch. One could have expected this relation as the parallel velocity, i.e., the velocity particle travels along the (stochastic) field lines, is proportional to pitch.

Since particle energy also affects its velocity, we could expect the energy to affect the transport in a similar way as pitch does. However, RE with $\mathcal{E} = 10$ MeV already has a parallel velocity of $0.998c$ so further increase in energy makes only a small difference in velocity. Figure 6.5 shows that energy does affect transport but the relationship is more complicated. First,

the number of confined particles decreases overall when energy is increased which is due to the orbit widening. Likewise, the boundary between non-confined and confined region is pushed closer to the plasma core. The orbit widening also leads to increase in first orbit losses which can be seen from Fig. 6.7. $\tilde{K}$ and $\tilde{D}$ should be evaluated more carefully to find out how these coefficients are affected by the particle energy.

The 1D-model seems to fare fairly well in all cases except for the case where RE energy is 100 MeV. Agreement is expected to be better if the model would also account for first orbit losses, and make better estimates for the fraction of confined particles. In all cases, the transport in the threshold regime is not accurately described which is due to the difficulty of evaluating $\tilde{K}$ and $\tilde{D}$ there as only a few particles are non-confined and the reflecting boundary is not accounted for in the evaluation process. Manually decreasing the value of $\tilde{D}$ in the threshold region led to results that were more similar to those given by ASCOT. The evaluation process would become more robust if the physical basis of the transport were understood. $\tilde{D}$ could be related to the Rechester-Rosenbluth diffusion coefficient, Eq. (2.1), but finding whether this is the case is left for future work. The exact physical process responsible for generating the drift remains unknown. To see whether diffusion alone is sufficient for modelling the transport, we substituted $\tilde{K} = 0$ in the 1D-model. However, these simulations failed to reproduce the transport given by ASCOT.

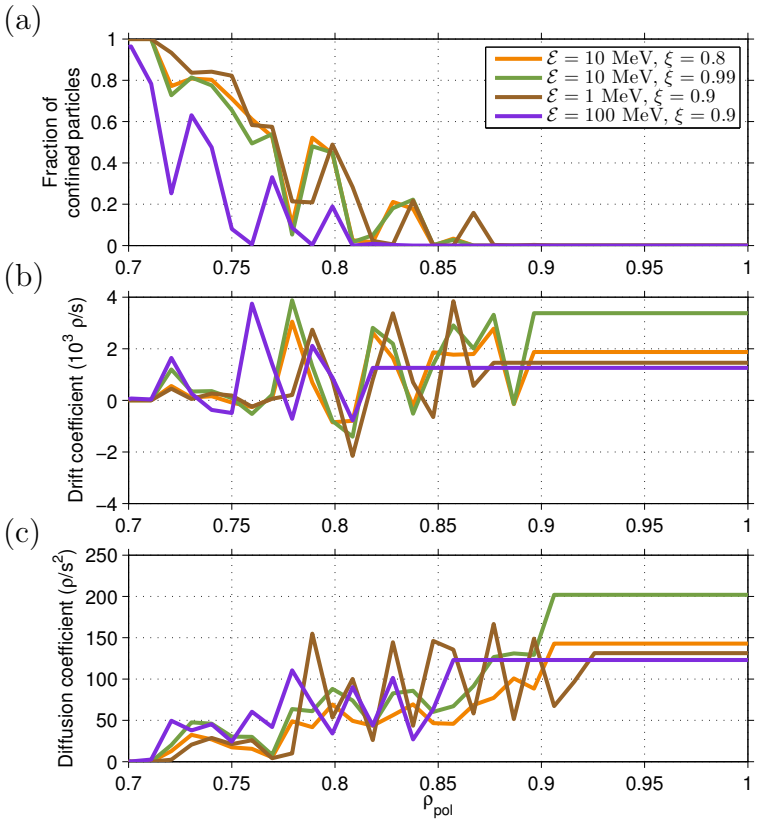

Figure 6.5: The fraction of confined particles and the transport coefficients for RE populations with different values for pitch and energy, evaluated with ASCOT. The influence of pitch can be seen by comparing the orange and green curves, and the effect of energy by comparing brown and violent ones. The lower pitch value leads to slightly lower values for the transport coefficients while the fraction of confined remains almost the same. The relationship between the transport coefficients and energy is more complex.

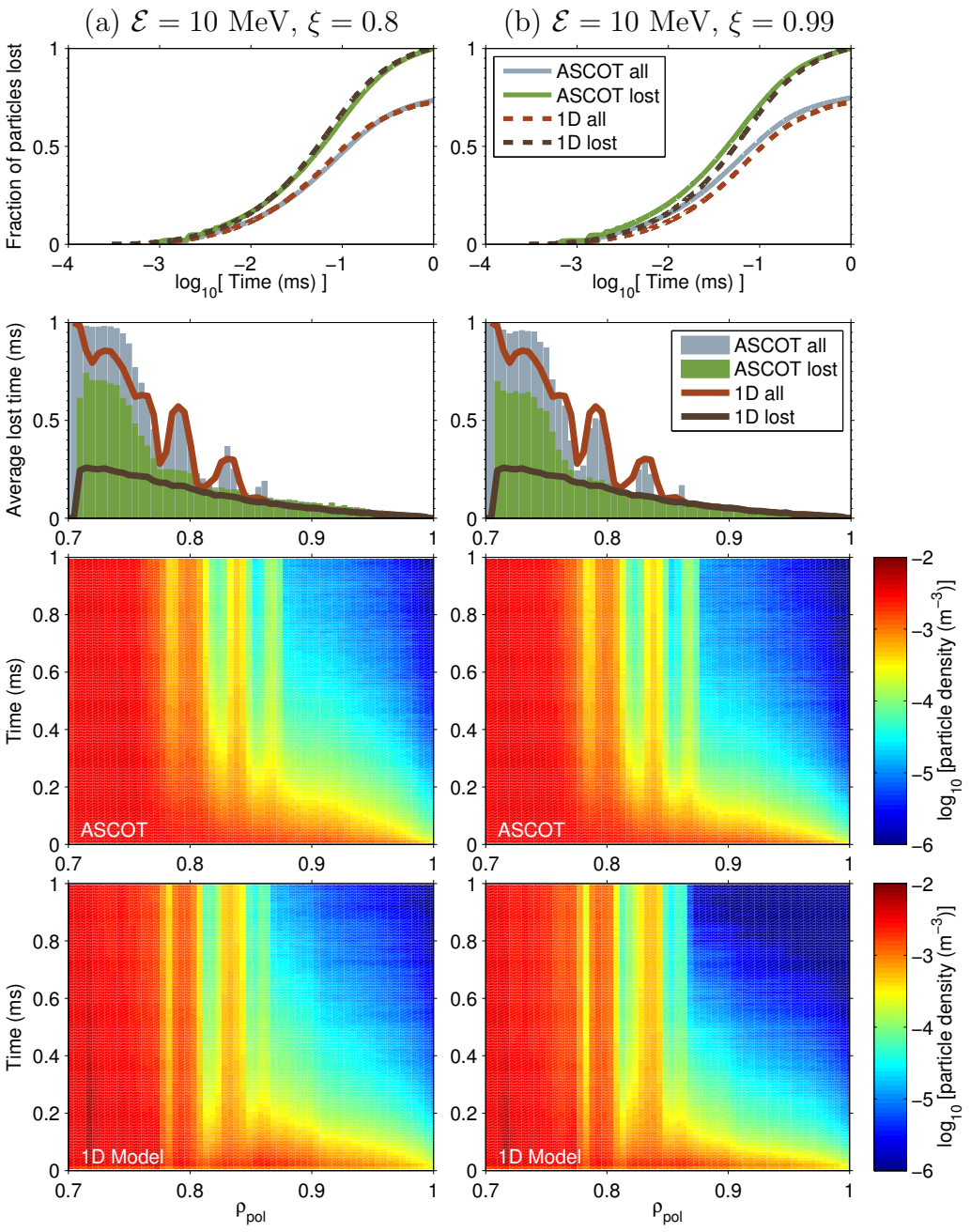

Figure 6.6: Comparison of RE transport and a benchmark of the 1D-model when RE *pitch* is altered while energy is kept constant. The lower pitch value leads to a slight increase in average loss times while otherwise the transport seems to be unaltered. 1D-model replicates well the results given by ASCOT in both cases.

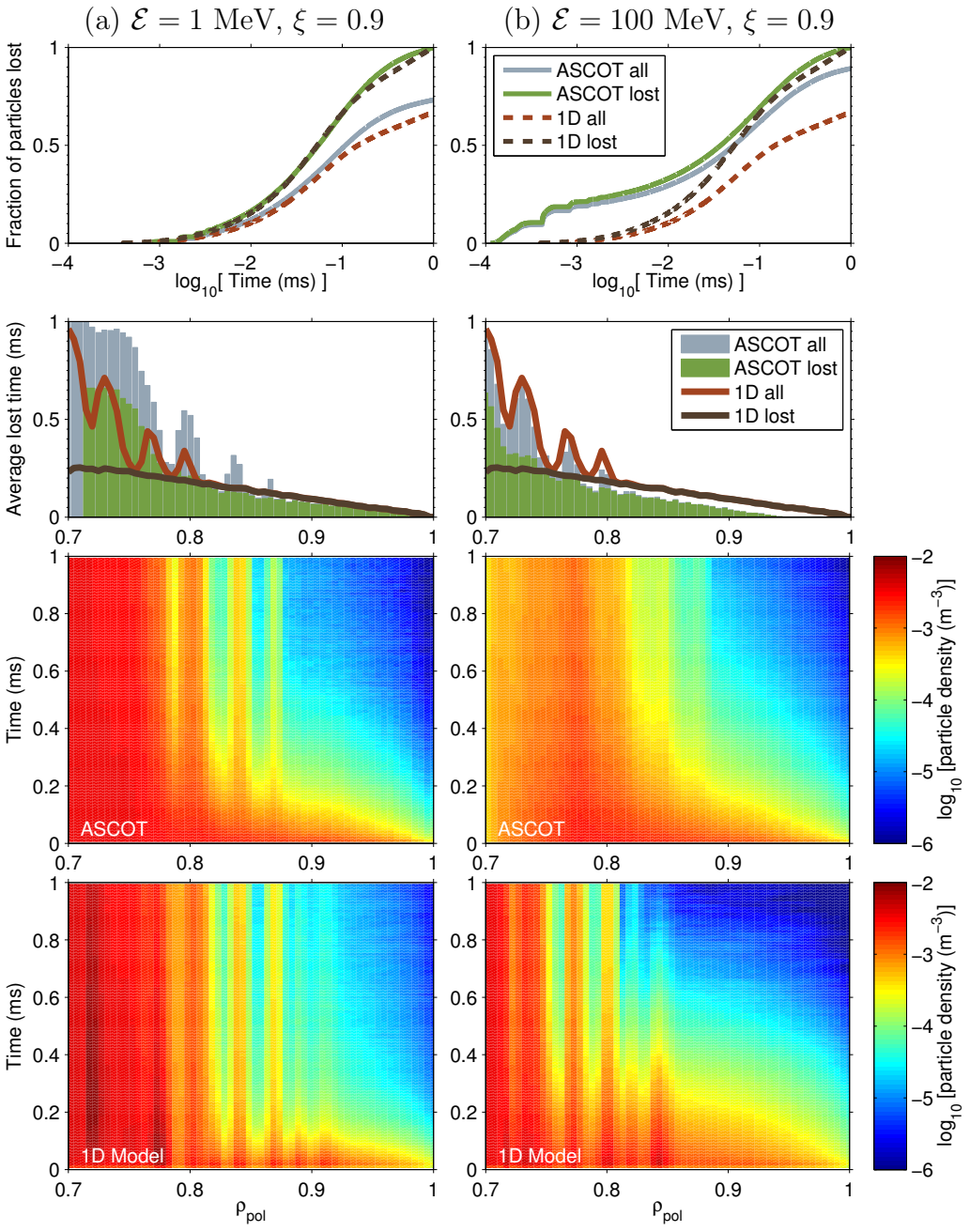

Figure 6.7: Comparison of RE transport and a benchmark of the 1D-model when RE *energy* is altered while pitch is kept constant. Increased energy causes more particles to be lost as well as increases the loss rate. The 1D-model has some succes in replicating the ASCOT results for REs with $\mathcal{E} = 1$ MeV but fails when the energy is 100 MeV.

Chapter 7

Summary and conclusions

The objective of this work was to develop numerical tools suitable for studying runaway electron (RE) losses. Orbit-following codes are unchallenged tools for investigating what physics processes are responsible for the losses as they can study particle trajectories in complex 3D magnetic fields. Therefore, orbit-following codes can provide valuable information in predicting whether a RE mitigation scheme will be eligible in practice. One of such a code, ASCOT, was upgraded to include relevant RE physics as a part of this thesis project. ASCOT was then used to gain a better understanding of RE transport in the presence of external magnetic perturbations which is a relevant issue considering mitigation of the disruption-generated REs. The REs born during a plasma disruption form an energetic beam that impacts the first wall if REs are left unmitigated. This thesis provides an overview of the RE phenomena during a plasma disruption together with the proposed RE mitigation techniques for ITER. One of the proposed mitigation methods is to create a magnetic field perturbation, with either gas injection or external coils, to suppress the RE avalanche. The avalanche is suppressed when REs are lost more rapidly than new ones are created by knock-on collisions.

ASCOT employs guiding center formalism to greatly speed-up the computations, thus facilitating simulations with a large number of test particles. In chapters 3 and 4, we performed a literature review on the guiding center formalism. The guiding center phase space is inherently noncanonical so we dedicated one section to review noncanonical Hamiltonian mechanics for readers that are unfamiliar with the subject. Many physical models, such as equations of motion and collision operator, are derived from first principles in the particle picture only and, therefore, they need to be transformed to guiding center phase space. This is accomplished with a guiding center transformation operators, based on the Lie transform perturbation method. The Fokker-Planck collision operator, and its relation to the Langevin equa-

tion, which is the stochastic differential equation upon which orbit-following Monte Carlo codes are based, were presented in chapter 3. We showed how, by transforming the Fokker-Planck equation from the particle phase space to the guiding center phase space, it is possible to include collisions and other non-Hamiltonian dynamics in the guiding center picture. The mathematical tools we gained from these discussions were put to use in chapter 4, where we showed how those are used to derive the relativistic Hamiltonian guiding center equations of motion in $(X, p_\parallel, \mu, \theta)$ coordinates. These equations were complemented by including also the relativistic collision operator and radiation reaction force. We used the relativistic Fokker-Planck coefficients evaluated for a Maxwellian plasma to calculate guiding center Fokker-Planck collision operator in (X, p, ξ, θ) coordinates. Using only the zeroth order terms from the guiding center transformation, the radiation reaction force, i.e., the Abraham-Lorentz-Dirac (ALD) force, was incorporated to Hamiltonian equations of motion as an extra force term.

ASCOT already contained the relativistic equations of motion, so implementing only the ALD force and relativistic collisions was necessary before RE simulations could take place. The implementation procedure was described in chapter 5. The implementation of the ALD force included only the zeroth order terms. Indeed, comparison of particle energy between full-orbit and guiding-center modes led to the conclusion that first order terms can be omitted in ITER magnetic fields. The relativistic pitch collision operator was found to differ from the nonrelativistic one by 1 % in RE relevant energies. Even though the difference is small, this could still affect the slowing down time significantly as pitch collisions also contribute to energy loss. At high energies, the pitch scattering slows the REs down via the ALD force. The pitch collision frequency was larger with the relativistic operator than with the nonrelativistic one. Chapter 5 also includes verification of the relativistic equations of motion, as well as the suitable error tolerance for the Cash-Karp integration method when simulating REs.

The retrofitted ASCOT was put to use in chapter 6 where collisionless RE transport in a stochastic magnetic field was studied. Finding a simple model for the collisionless radial transport would benefit many other codes that study RE populations as a whole but are spatially limited to only radial coordinate. Omitting collisions and the ALD force, it was found out that satisfactory results are achieved when transport is modelled with a combination of drift and diffusion. Corresponding transport coefficients are evaluated by tracing the RE trajectories with ASCOT in a given background. These trajectories are also used in finding the fraction of confined particles at each flux surface, so that the transport model could also account for these. The transport model, dubbed as '1D-model', was verified by comparing radial re-

distribution of 1×10^5 REs, placed in the stochastic region, with both ASCOT and the 1D-model. The method of evaluating transport coefficients still needs further development but, nevertheless, the results given by 1D-model agreed fairly well with those given by full-scale ASCOT simulations. The simulations were repeated for RE populations with different energy and pitch values to find out how these parameters affect the transport and to further test the 1D-model. Changing particle pitch did not result in significantly different transport, although the inspection was restricted to passing particles. If the orbit topology is not altered, the particle pitch affects mainly the amount of velocity that is parallel to the field, i.e., responsible for transport, so linear dependence between pitch and transport is expected. On the other hand, the particle energy had significant effect on the transport behavior, and the 1D-model did not manage to replicate highly energetic (100 MeV) RE transport well. However, the shortcoming of the 1D-model is due to method of extracting transport coefficients from ASCOT results. RE transport itself is affected by the RE energy mainly because less particles are in confined orbits when energy is increased.

The 1D-model would benefit if an analytical dependence between radial position and transport were to be found. This would make the procedure of evaluating transport coefficients more robust, as identifying meaningful transport coefficients near the edge is difficult since there REs are lost during few poloidal orbits. Additionally, the boundary between the confined and non-confined region is assumed to be reflecting. Near this boundary, the method used for calculating the transport coefficients overestimates RE transport. Future developments should also include collisions and the ALD force, along with the electric field, to find out how these affect the transport.

ASCOT is now equipped with relevant physics to study RE phenomena in plasma disruptions. The physics that are included are compatible with special relativity, so that electrons with energies of several MeVs can be simulated accurately. ASCOT is not limited to evaluation of the transport coefficients as it can simulate RE population, at least in principle, from birth to grave. For example, REs could be generated during simulation via Dreicer mechanism. However, this is probably computationally too expensive as this scheme would require simulating a large number of thermal particles representing the Maxwellian bulk of which only a small fraction would become RE during a time corresponding to the current quench. On the other hand, RE generation due to avalanche would require implementing knock-on collisions. Mimicking hot-tail mechanism is impossible in ASCOT as the code assumes steady-state conditions. Even though it is in principle possible to generate REs during the simulation, the most feasible way is to give RE population as an input. The detailed wall model and the possibility of using an arbitrary

magnetic field makes ASCOT a powerful tool for estimating hot-spots and wall loads due to RE beam.

This work only considered RE mitigation via magnetic perturbations. Since the method of increasing collisionality via impurity injection has gained support, ASCOT should be made suitable for studying also this method. The only missing piece of relevant physics is bremsstrahlung which should be straightforward to implement. After that, ASCOT will be useful for studying not only RE losses, but also RE dynamics. Increased pitch scattering due to impurities could lead to the ALD force preventing REs from achieving high energies. Furthermore, some REs could scatter to trapped particle regime where the electric field no longer accelerates them. If this were the case, RE mitigation would become much less of a threat for successful ITER operation.

Bibliography

[1] R. Gross. *Fusion energy.* John Wiley and Sons,New York, NY, 1984.

[2] K. Ikeda. ITER on the road to fusion energy. *Nuclear Fusion*, 50(1):014 002, 2010. doi:10.1088/0029-5515/50/1/014002.

[3] S. Ichimaru. *Basic Principles of Plasma Physics: A Statistical Approach.* W. A. Benjamin, 1973. ISBN 9780805387537.

[4] H. Dreicer. Electron and ion runaway in a fully ionized gas. I. *Physical Review*, 115(2):238, 1959.

[5] F. Andersson. *Runaway Electrons in Tokamak Plasmas.* Doktorsavhandlingar vid Chalmers Tekniska Högskola: Chalmers Tekniska Högskola. Department of Electromagnetics, School of Electrical Engineering, Chalmers University of Technology, 2003. ISBN 9789172913615.

[6] A. Stahl, E. Hirvijoki, J. Decker, O. Embréus, and T. Fülöp. Effective Critical Electric Field for Runaway-Electron Generation. *Phys. Rev. Lett.*, 114:115 002, 2015. doi:10.1103/PhysRevLett.114.115002.

[7] H. M. Smith, T. Fehér, T. Fülöp, K. Gál, and E. Verwichte. Runaway electron generation in tokamak disruptions. *Plasma Physics and Controlled Fusion*, 51(12):124 008, 2009.

[8] J. A. Heikkinen, S. K. Sipilä, and T. J. H. Pättikangas. Monte Carlo simulation of runaway electrons in a toroidal geometry. *Computer Physics Communications*, 76(2):215–230, 1993. ISSN 0010-4655. doi: 10.1016/0010-4655(93)90133-W.

[9] P. Helander, L.-G. Eriksson, and F. Andersson. Suppression of runaway electron avalanches by radial diffusion. *Physics of Plasmas (1994-present)*, 7(10):4106–4111, 2000.

[10] S. Bozhenkov, M. Lehnen, K. Finken et al. Generation and suppression of runaway electrons in disruption mitigation experiments in TEXTOR. *Plasma physics and controlled fusion*, 50(10):105 007, 2008.

[11] T. Fehér, H. Smith, T. Fülöp, and K. Gál. Simulation of runaway electron generation during plasma shutdown by impurity injection in ITER. *Plasma Physics and Controlled Fusion*, 53(3):035 014, 2011.

[12] F. Saint-Laurent, G. Martin, T. Alarcon et al. Overview of runaway electron control and mitigation experiments on Tore Supra and lessons learned in view of ITER. *Fusion Science and Technology*, 64(4):711–718, 2013.

[13] F. C. Schuller. Disruptions in tokamaks. *Plasma Physics and Controlled Fusion*, 37(11A):A135, 1995.

[14] P. Taylor, A. Kellman, T. Evans et al. Disruption mitigation studies in DIII-D. *Physics of Plasmas (1994-present)*, 6(5):1872–1879, 1999.

[15] G. Papp, M. Drevlak, G. I. Pokol, and T. FÃ$\frac{1}{4}$lÃ¶p. Energetic electron transport in the presence of magnetic perturbations in magnetically confined plasmas. *Journal of Plasma Physics*, 81, 2015. ISSN 1469-7807. doi:10.1017/S0022377815000537.

[16] A. Stahl, M. Landreman, G. Papp, E. Hollmann, and T. Fülöp. Synchrotron radiation from a runaway electron distribution in tokamaks. *Physics of Plasmas (1994-present)*, 20(9):093 302, 2013.

[17] H. Smith, P. Helander, L.-G. Eriksson et al. Runaway electrons and the evolution of the plasma current in tokamak disruptions. *Physics of Plasmas (1994-present)*, 13(10):102502, 2006. doi:http://dx.doi.org/10.1063/1.2358110.

[18] E. Hirvijoki, O. Asunta, T. Koskela et al. ASCOT: Solving the kinetic equation of minority particle species in tokamak plasmas. *Computer Physics Communications*, 185(4):1310–1321, 2014. ISSN 0010-4655. doi:10.1016/j.cpc.2014.01.014.

[19] V. Riccardo, S. Walker, and P. Noll. Parametric analysis of asymmetric vertical displacement events at JET. *Plasma Physics and Controlled Fusion*, 42(1):29, 2000.

[20] D. Whyte, T. Jernigan, D. Humphreys et al. Mitigation of tokamak disruptions using high-pressure gas injection. *Physical review letters*, 89(5):055 001, 2002.

[21] S. Bozhenkov, K. Finken, M. Lehnen et al. Disruption mitigation by massive gas injection at TEXTOR. In *34th EPS Conference on Plasma Physics, Warsaw (Poland)*. 2007.

[22] M. Lehnen, A. Alonso, G. Arnoux et al. Disruption mitigation by massive gas injection in JET. *Nuclear Fusion*, 51(12):123 010, 2011.

[23] M. Sugihara, M. Shimada, H. Fujieda et al. Disruption scenarios, their mitigation and operation window in ITER. *Nuclear Fusion*, 47(4):337, 2007.

[24] S. Putvinski. Runaway electrons in tokamaks and their mitigation in ITER. In *US-BPO Disruptions Workshop, San Diego*. 2012.

[25] M. Rosenbluth and S. Putvinski. Theory for avalanche of runaway electrons in tokamaks. *Nuclear Fusion*, 37(10):1355, 1997.

[26] H.-W. Bartels. Impact of runaway electrons. *Fusion engineering and design*, 23(4):323–328, 1994.

[27] M. Forster. *Runaway electrons in disrupions and perturbed magnetic topologies of Tokamak plasmas*. Ph.D. thesis, Düsseldorf, Heinrich-Heine-Universität, Diss., 2012, 2012.

[28] M. Lehnen, S. Abdullaev, G. Arnoux et al. Runaway generation during disruptions in JET and TEXTOR. *Journal of Nuclear Materials*, 390:740–746, 2009.

[29] G. Papp, M. Drevlak, T. Fülöp, P. Helander, and G. Pokol. Runaway electron losses caused by resonant magnetic perturbations in ITER. *Plasma Physics and Controlled Fusion*, 53(9):095 004, 2011.

[30] E. Nilsson, J. Decker, Y. Peysson et al. Kinetic modelling of runaway electron avalanches in tokamak plasmas. *Plasma Physics and Controlled Fusion*, 57(9):095 006, 2015.

[31] G. Papp, T. Fülöp, T. Fehér et al. The effect of ITER-like wall on runaway electron generation in JET. *Nuclear Fusion*, 53(12):123 017, 2013.

[32] L.-G. Eriksson and P. Helander. Simulation of runaway electrons during tokamak disruptions. *Computer Physics Communications*, 154(3):175–196, 2003.

[33] A. Rechester and M. Rosenbluth. Electron heat transport in a Tokamak with destroyed magnetic surfaces. *Physical Review Letters*, 40(1):38, 1978.

[34] J. Cary and A. Brizard. Hamiltonian theory of guiding-center motion. *Rev. Mod. Phys.*, 81:693–738, 2009. doi:10.1103/RevModPhys.81.693.

[35] A. Brizard. *Nonlinear gyrokinetic tokamak physics*. Ph.D. thesis, Princeton University, 1990.

[36] E. Hirvijoki. *Theory and models for Monte Carlo simulations of minority particle populations in tokamak plasmas*. Ph.D. thesis, Aalto University, School of Science, 2014.

[37] E. Hirvijoki, A. Brizard, A. Snicker, and T. Kurki-Suonio. Monte Carlo implementation of a guiding-center Fokker-Planck kinetic equation. *Physics of Plasmas*, 20(9):092505, 2013. doi:10.1063/1.4820951.

[38] J. R. Cary and R. G. Littlejohn. Noncanonical Hamiltonian mechanics and its application to magnetic field line flow. *Annals of Physics*, 151(1):1–34, 1983.

[39] J. M. Greene. Noncanonical Hamiltonian mechanics. In *Mathematical Methods in Hydrodynamics and Integrability in Dynamical Systems*, volume 88, pp. 91–97. AIP Publishing, 1982.

[40] A. J. Brizard and N. Tronko. Equivalent representations of higher-order Hamiltonian guiding-center theory. *arXiv preprint arXiv:1205.5772*, 2012.

[41] K. Sekimoto. *Stochastic energetics*, volume 799. Springer, 2010.

[42] X. Tao, A. Chan, and A. Brizard. Hamiltonian theory of adiabatic motion of relativistic charged particles. *Physics of Plasmas*, 14(9):092107, 2007. doi:10.1063/1.2773702.

[43] E. Hirvijoki, J. Decker, A. J. Brizard, and O. Embreus. Guiding-centre transformation of the radiation-reaction force in a non-uniform magnetic field. *Journal of Plasma Physics*, 81, 2015. ISSN 1469-7807. doi:10.1017/S0022377815000744.

[44] O. Pike and S. Rose. Dynamical friction in a relativistic plasma. *Physical Review E*, 89(5):053 107, 2014.

[45] J. Jimenez and I. Campos. Models of the classical electron after a century. *Journal of Genetic Counseling*, 12(2):127–146, 1999.

[46] F. L. Hinton. Collisional transport in plasma. *Handbook of Plasma Physics*, 1:147, 1983.

[47] B. J. Braams and C. F. Karney. Conductivity of a relativistic plasma. *Phys. Fluids B*, 1(7), 1989.

[48] T. Koskela, O. Asunta, E. Hirvijoki, T. Kurki-Suonio, and S. Äkäslompolo. ITER edge-localized modes control coils: the effect on fast ion losses and edge confinement properties. *Plasma Physics and Controlled Fusion*, 54(10):105 008, 2012. doi:10.1088/0741-3335/54/10/105008.

[49] A. Salmi, T. Johnson, V. Parail et al. ASCOT Modelling of Ripple Effects on Toroidal Torque. *Contributions to Plasma Physics*, 48(1-3):77–81, 2008. ISSN 1521-3986. doi:10.1002/ctpp.200810013.

[50] A. Snicker, T. Kurki-Suonio, and S. K. Sipilä. Realistic Simulations of Fast-Ion Wall Distribution Including Effects Due to Finite Larmor Radius. *Plasma Science, IEEE Transactions on*, 38(9):2177 –2184, 2010. ISSN 0093-3813. doi:10.1109/TPS.2010.2056705.

[51] J. R. Cash and A. H. Karp. A variable order Runge-Kutta method for initial value problems with rapidly varying right-hand sides. *ACM Transactions on Mathematical Software (TOMS)*, 16(3):201–222, 1990.

[52] R. Zhang, J. Liu, H. Qin et al. Volume-preserving algorithm for secular relativistic dynamics of charged particles. *Physics of Plasmas (1994-present)*, 22(4):044 501, 2015.

[53] J. Burkardt. Source Codes in Fortran90. `http://people.sc.fsu.edu/~jburkardt/f_src/f_src.html`. Accessed: 2015-08-07.

[54] P. E. Kloeden and E. Platen. Higher-order implicit strong numerical schemes for stochastic differential equations. *Journal of statistical physics*, 66(1-2):283–314, 1992.

[55] S. Äkäslompolo, O. Asunta, T. Bergmans et al. Calculating the 3D magnetic field of ITER for European TBM studies. *Fusion Engineering and Design*, 2015.

[56] A. Boozer and G. Kuo-Petravic. Monte Carlo evaluation of transport coefficients. *Physics of Fluids*, 24(5):851–859, 1981. doi:10.1063/1.863445.